Simulation of Multi-Injector H2-O2 Rocket Combustion Instability

Yalu Zhu, Feng Liu and William A. Sirignano

Published Online: 1 Oct 2025 • https://doi.org/10.2514/1.J065542

Abstract

An efficient large-eddy simulation code has been developed to simulate combustion instabilities in a hydrogen–oxygen (H_2-O_2) rocket engine combustion chamber with multiple injectors. The code uses multiblock structured hexahedral grids with a patched-grid interface between the combustion chamber and the injection ports, which allowed improved accuracy with a relatively small number of total grid points compared to the use of unstructured tetrahedral or prism grids. Both the flow in the fuel/oxygen injection system and the combustion chamber are simulated and directly coupled through the patched interface method. A half model of an experimental rocket combustor chamber with 42 hydrogen–oxygen injection ports is sufficient. A one-step finite-rate chemistry is employed to capture the dynamics of chemical reaction. Modal analysis methods based on fast Fourier transform and dynamic mode decomposition are used to analyze the computed unsteady pressure field. Primary acoustic waves, including three longitudinal modes, two standing tangential modes, and one radial mode in the combustion chamber, are identified without any triggering. Also, an injection-coupled chugging frequency is clearly identified. The first tangential mode is identified as the dominant self-excited instability mode, in agreement with the experimental data for the combustor. The spatial distribution of the mode shapes in the combustion chamber is explained, accounting for sound speed variations in the axial direction. Analysis of the interaction between the longitudinal wave system within the injection ports and those in the combustion chamber reveals an important feature of the combustion instability. When a natural frequency of the combustion chamber occurs as a harmonic of that of the injection ports, waves from the chamber travel into the injection ports, inducing resonant oscillations within the ports, which in turn causes oscillations of the heat release rate in the reaction zone downstream of the injection plate. Since this fluctuation of heat release is in sync with the

chamber pressure oscillations, it can heighten the Rayleigh index, strengthening the combustion instability. This coupling mechanism has not been previously analyzed mathematically, but it is found to agree with existing experimental and computational data and may provide guidance in practical design to avoid rocket engine combustion instability.

Nomenclature

C_p	specific heat capacity at constant pressure
c	speed of sound
cc	combustion chamber
E	total energy
f	frequency
h	sensible enthalpy
h^0	enthalpy of formation at reference temperature T_{ref}
$\boldsymbol{j}$	diffusive flux of species
N	total number of species

Nomenclature

ox	oxygen injector
Pr	Prandtl number
p	pressure
$\dot{Q}$	heat release rate of chemical reaction
$\boldsymbol{q}$	heat flux
R	gas constant
R_0	universal gas constant, $R_0 = 8.3145\ \mathrm{J/mol/K}$
r	radial coordinate
Sc	Schmidt number
T	temperature

Nomenclature

T_{ref}	reference temperature, $T_{\text{ref}} = 298.15\ \text{K}$
t	time
$\boldsymbol{V}$	velocity vector
W	molecular weight
x	axial coordinate from the chamber entrance
Y	mass fraction
θ	azimuthal coordinate
μ	viscosity coefficient
ρ	density
$\boldsymbol{\tau}$	viscous stress tensor

Nomenclature

$\dot{\omega}$	net production rate due to chemical reaction
$(\cdot)_i$	quantity of species *i*
$(\cdot)_T$	quantity of turbulence
$(\cdot)^T$	transpose of quantity
$\overline{(\cdot)}$	time-averaged quantity
$(\cdot)_0$	quantity in stagnation state
1L	the first longitudinal mode
1R	the first radial mode
1T	the first standing tangential mode
2L	the second longitudinal mode

Nomenclature	
2R	the second radial mode
2T	the second standing tangential mode
3L	the third longitudinal mode
3T	the third standing tangential mode
7L	the seventh longitudinal mode

I. Introduction

Arocket engine contains several volumes with rigid walls, like propellant manifolds, injectors, combustion chambers, and nozzles. These component volumes have specific resonant frequencies depending on their geometries and fluid properties. Unstable acoustic oscillations with their resonant frequencies arise in the engine, excited by turbulence or combustion. This phenomenon is called combustion instability. Whether combustion instability happens or not can be learned by experimental measurements [1–3]. However, if combustion happens in a complex system operated at a high pressure level, like the case in a real rocket engine, it is difficult to systematically study the combustion instability by experiments due to the expense and the limitation of current measurement techniques.

Combustion instability can induce a periodic modulation to the heat release rate of the combustion process. Rayleigh [4] postulated that, if the pressure fluctuation is in phase with the heat release rate over a period of oscillation, energy transfers from the combustion chemistry into the acoustic pressure oscillation, resulting in a rapid increase of the pressure oscillation amplitude. This can cause undesirable effects on thrust or even destruction of the whole engine [5]. The Rayleigh index is based on a cyclic integral of the product of mass burning rate and pressure fluctuations and related to the source term in the balance equation of linear acoustic energy, as expressed in a mathematical way in Refs. [6–10]. A practical use of this equation requires a knowledge of the unsteady acoustic response

of combustion.

For three-quarters of a century since the pioneering days for the development of liquid-propellant rocket engines (LPREs) and the associated theoretical explanation of combustion instability, there have been attempts to connect properly the characteristic combustion time (related to the reciprocal of mass burning rate) with the characteristic times for both the acoustic oscillations (e.g., periods of oscillation) and the flow dynamics (e.g., reciprocals of strain rates and vorticity). Crocco and Cheng [6] and Reardon et al. [11,12] used the sensitive time-lag theory together with linear analysis of the flow dynamics. This approach introduced two parameters, interaction index n and sensitive time lag τ, which were intended to be determined experimentally based on propellant choices and injector design. Interaction between the acoustics and combustion was clearly stated with their postulate, although the many scientific details of the combustion process were hidden. This theory was then extended to address nonlinear acoustics by Sirignano [13], Zinn [14], and Mitchell et al. [15]. These extensions explained the common practical threat of triggered nonlinear combustion instability by identifying both stable and unstable limit cycles. However, the sensitive time-lag theory could not address directly without empiricism, the many details of combustion and its connections with flow dynamics that became more accessible as computational fluid dynamics emerged.

With the development of high-performance computing, it is possible to address the combustion instability issue in a rocket engine by using numerical methods that solve the whole nonlinear dynamic system coupled with turbulent flow, combustion, and acoustics [8]. Due to the unsteady and nonlinear nature of this problem, high-fidelity modeling approaches, such as large-eddy simulation (LES) and detached-eddy simulation (DES), along with appropriate chemistry models, are powerful candidates for the numerical simulation. There are several numerical studies on combustion instabilities in single-injector rocket combustors. The combustion instability in the continuously variable resonance combustor (CVRC), a single-coaxial-injector, low-pressure, methane–oxygen combustor experimentally studied at Purdue University [1–3], has been numerically investigated by many authors [16–25]. Three different instability regimes produced by different oxidizer post lengths, i.e., fully unstable, semistable, and completely stable regimes, were examined. Both axisymmetric and three-dimensional (3D) LES [16,17] and DES [18–25] have been conducted to investigate the sensitivity to various operating parameters. The comparisons between axisymmetric and 3D results suggested that 3D effects cannot be ignored [16,17]. These studies also confirmed the presence of multiple longitudinal acoustic modes in the combustor and showed that primary modes in the combustor are predicted in a reasonable agreement with the experimental data.

In single-injector combustors, only longitudinal mode coupling occurs between the injector system and the combustion chamber. In contrast, multi-injector combustors, which more closely resemble real rocket engines, can capture the coupled acoustic instabilities between transverse modes in the chamber and longitudinal modes in the injectors. An experimental 42-injector hydrogen–oxygen liquid rocket combustor, designated Brennkammer D (BKD), was developed for studying self-excited high-frequency combustion instabilities at the German Aerospace Center (DLR) [26–31]. It has been used as a benchmarking test case in the Rocket Engine Stability Initiative (REST) modeling workshops

[32–34]. The combustion instabilities in the BKD engine were numerically analyzed not only by using the linear Euler equations or Helmholtz equation coupled with the Reynolds-averaged Navier–Stokes (RANS) equations [35,36] but also by using LES [32,33,37–40]. Urbano et al. [37–39] performed LES for both stable and unstable operating points in BKD and found that the overall acoustic activities in the chamber are strongly coupled with the oxidizer injectors, similar to the case in the single-injector CVRC configuration. Hwang et al. [40] conducted LES of unstable combustion in it, particularly focusing on the jet dynamics of a single injector. Schmitt et al. [32,33] investigated the effects of fuel injection temperature and grid resolution on acoustic instabilities in BKD. It was found that the fuel injection temperature plays an important role in the thermo-acoustic stability of the chamber, and a fine enough mesh is necessary to obtain a favorably comparable solution with the experimental measurement in terms of frequency and amplitude of the dominant mode. Previous computational studies typically predicted triggered transverse oscillations in BKD [37–40], which did not match the self-excited behavior observed in experiments [26]; self-excited instability was only obtained when the fuel injection temperature was increased [32,33]. In these computations, unstructured tetrahedral or prismatic grids were generated for the complete propellant injection system, including domes, throttles, and the whole fuel injectors, resulting in enormous grid sizes and thus high computational costs. Xiong et al. [41–43] and Zhan et al. [44] simulated the nonlinear combustion instability in a methane–oxygen experimental engine with 10, 19, 30, and 82 coaxial injectors using DES. The 82-injector case simulated a Rocketdyne experiment [45]. It was demonstrated that the longitudinal and transverse modes in the chamber can be captured by using a simplified propellant injection system. A version of the open-source software OpenFOAM, which is based on unstructured grids, was used in these studies [40–44].

There are several ways to introduce the details of chemistry into simulations of combustion instabilities in rocket engines. Combustion for the BKD combustor has typically been modeled under the assumption of chemical equilibrium [32,33,37–39]. As a result, the characteristic chemical timescale is zero, and the characteristic combustion timescale only depends on flow mixing. We prefer to avoid this approach because it bypasses issues of flammability, extinction, and re-ignition, which are relevant to turbulent combustion. Thus, we see the need to address in some way finite-rate chemical kinetics on the resolved scale for treatments with RANS or LES approaches. Since detailed kinetic mechanisms become computationally expensive for turbulent flow analysis, one-step chemical kinetics was typically used. It was used to study nonlinear longitudinal combustion instability with shock wave formations in an experimental rocket engine where premixed propellants were introduced through porous injectors [46]. Since premixing occurred before injection, the aspects where mixing is affected by the fluid dynamics or acoustics were not considered. More recently, Xiong et al. [41–43] and Zhan et al. [44] used one-step chemical kinetics at the resolved scale. A comparison with the experimental engine indicated some overprediction of the burning rate. Alternatively, flamelet models computed offline can provide lookup tables or neural networks for the primary fluid dynamics computations. Interactions between chemistry and subgrid mixing were incorporated by Nguyen et al. [21], Nguyen and Sirignano [22,23], and Shadram et al. [24,25] using the flamelet progress-variable model [47] to study the combustion instability in the CVRC configuration. Reasonable agreement was found on the acoustical behaviors. Zhan et al. [44] also used the flamelet

progress-variable model for a 10-injector engine and made comparisons with results for the method with one-step kinetics at the resolved scale. While the progress-variable method provides a connection between the chemistry and small-scale molecular mixing through offline calculation and the resolved-scale fluid and thermal dynamics, it connects weakly to critical details of a turbulent flow. For example, the effects of vorticity are not represented, and the issues of scaling through the cascade of turbulent kinetic energy are not well represented.

While previous studies have demonstrated the utility of numerical simulation in predicting combustion instabilities in rocket engines, the computational efficiency and accuracy are still desired to be improved. First, the complexity of the propellant injection system can be reduced by omitting components, such as domes, throttles, and the upstream fuel injector section. In consideration of the azimuthal periodicity of both geometry and flow, the full-cylinder engine can be further simplified into a partial-cylinder configuration, reducing computational costs while preserving the essential physics. A traveling tangential mode will not be captured here. Second, structured hexahedral grids, along with a careful treatment on the interface between components, offer significant advantages over unstructured tetrahedral or prismatic grids, including ease of generation for individual engine components and better control over crucial grid qualities such as orthogonality and skewness. These attributes enhance computational efficiency and improve solution accuracy. Finally, in contrast to the flamelet models based on equilibrium assumption [32,33,37–39], a finite-rate chemistry model, although it lacks a direct closure for turbulence–chemistry interactions, can better capture the dynamic feedback process between combustion and acoustic oscillations by resolving the reaction time explicitly [41–43]. This also reduces computational costs, particularly memory costs, by focusing only on the essential reaction products and eliminating the need for a lookup table. Here, we address the BKD configuration [26–31] using one-step kinetics in this initial work with the intention for the future to use improved modeling as it develops to allow relatively inexpensive computation using offline computations with considerations of detailed chemistry, proper treatment of scaling related to the cascade of turbulent kinetic energy, and the consideration of both strain rates and vorticity on the burning rate. References [48–53] provide an indication for future directions.

To address the aforementioned issues of simulating combustion instabilities in a rocket combustor with multiple injectors, we have developed an in-house code to solve the unsteady, compressible, multicomponent, reacting Navier–Stokes equations with LES turbulence models by using a finite-volume method on multiblock structured grids. The time scales of both flow and reaction are resolved by using a finite-rate chemistry model. In this study, the code is applied to simulate the reacting flow in the BKD rocket combustor and investigate the mechanism of the combustion instabilities, utilizing a half-cylinder configuration with a simplified propellant injection system. The governing equations and numerical methods are presented in Sec. II, along with a volume-weighted interpolation method for transferring flow variables across the patched-grid interface between the chamber and injectors. The time- and space-averaged results in the chamber are presented in Sec. III.A. The unsteady flowfields and the pressure frequency spectrum are discussed in Sec. III.B. The primary longitudinal, tangential, and radial acoustic mode shapes in the chamber and nozzle are analyzed in Sec. III.C. The mechanism of the combustion instabilities is discussed in Sec. III.D. Conclusions are given in Sec. IV.

II. Numerical Methods

A. Governing Equations

The governing equations used in this study are the three-dimensional, unsteady, compressible, multicomponent Navier–Stokes equations, expressed by the transport equations for partial density of each species in a mixture with *N* species, and momentum and energy of the mixture.

$$\frac{\partial(\rho Y_i)}{\partial t} + \nabla \cdot (\rho Y_i \boldsymbol{V}) = -\nabla \cdot \boldsymbol{j}_i + \dot{\omega}_i, \quad i = 1, 2, \ldots, N \tag{1a}$$

$$\frac{\partial(\rho \boldsymbol{V})}{\partial t} + \nabla \cdot (\rho \boldsymbol{V}\boldsymbol{V}) = -\nabla p + \nabla \cdot \boldsymbol{\tau} \tag{1b}$$

$$\frac{\partial(\rho E)}{\partial t} + \nabla \cdot (\rho E \boldsymbol{V}) = -\nabla \cdot (p\boldsymbol{V}) + \nabla \cdot (\boldsymbol{V} \cdot \boldsymbol{\tau}) - \nabla \cdot \boldsymbol{q} + \dot{Q} \tag{1c}$$

A perfect gas is assumed.

$$p = \rho R T \tag{2}$$

where *R* is the gas constant of the mixture, computed by the mass-weighted summation of the gas constant of each species R_i, with $R_i = R_0/W_i$. The total energy *E* is expressed by

$$E = h - \frac{p}{\rho} + \frac{1}{2}\boldsymbol{V} \cdot \boldsymbol{V} \tag{3}$$

with

$$h = \sum_{i=1}^{N} Y_i h_i, \qquad h_i = \int_{T_{\text{ref}}}^{T} C_{p,i}\, \mathrm{d}T \tag{4}$$

where $C_{p,i}$ is a function of temperature given by the empirical polynomial formula of NASA [54] for each species. The heat release rate (HRR), $\dot{Q}$, on the right-hand side of the energy equation is given by (5)

$$\dot{Q} = -\sum_{i=1}^{N} \dot{\omega}_i h_i^0$$

The transport properties in Eq. (1) are given by

$$\boldsymbol{\tau} = 2(\mu + \mu_T)\left[\boldsymbol{S} - \tfrac{1}{3}(\nabla \cdot \boldsymbol{V})\boldsymbol{I}\right], \quad \boldsymbol{S} = \tfrac{1}{2}[\nabla \boldsymbol{V} + (\nabla \boldsymbol{V})^T] \tag{6a}$$

$$\boldsymbol{j}_i = -\left(\tfrac{\mu}{\mathrm{Sc}_i} + \tfrac{\mu_T}{\mathrm{Sc}_T}\right)\nabla Y_i \tag{6b}$$

$$\boldsymbol{q} = -\left(\tfrac{\mu}{Pr} + \tfrac{\mu_T}{Pr_T}\right)\left(\nabla h - \textstyle\sum_{i=1}^{N} h_i \nabla Y_i\right) + \textstyle\sum_{i=1}^{N} h_i \boldsymbol{j}_i \tag{6c}$$

where $\boldsymbol{I}$ is the Kronecker tensor. The molecular viscosity μ is computed by the mass-weighted summation of the molecular viscosity of each species given by Sutherland's law [55]. The wall-adapting local eddy-viscosity (WALE) model [56] is adopted to determine the turbulent viscosity μ_T. The Schmidt number of species i, Sc_i, and the Prandtl number Pr are both set as 1.0. Their effects are expected to be negligible compared to turbulent diffusion. The turbulent Schmidt number Sc_T and the turbulent Prandtl number Pr_T are both set as 0.6, the same as the choices of Schmitt et al. [32,33] and Urbano et al. [37,38]. The last term in Eq. (6c) stands for the energy transport due to mass diffusion of each species with different enthalpy.

The combustion of hydrogen ($\mathrm{H_2}$) in oxygen ($\mathrm{O_2}$) is modeled by the one-step global reaction mechanism:

$$2\mathrm{H_2} + \mathrm{O_2} \rightarrow 2\mathrm{H_2O} \tag{7}$$

where only the final product, water vapor ($\mathrm{H_2O}$), is tracked besides the fuel and oxidizer. The reaction rate is given by the modified Arrhenius expression combined with the law of mass action:

$$\varepsilon = AT^{\beta}\mathrm{e}^{-E_a/(R_0T)}C_{\mathrm{H_2}}^{a}C_{\mathrm{O_2}}^{b} \tag{8}$$

where $C_i = \rho Y_i/W_i$ is the molar concentration of species i. According to Marinov et al. [57], $A = 9.0 \times 10^9\ \ (\mathrm{mol/m^3})^{1-a-b}/\mathrm{s/K}^{\beta}$, $\beta = 0$, $E_a = 146.4\ \ \mathrm{kJ/mol}$, $a = 1.0$, and $b = 0.5$. The net production rate of species *i* by the chemical reaction is computed by

$$\dot{\omega}_i = W_i(v_i'' - v_i')\varepsilon \tag{9}$$

where v_i' is the stoichiometric coefficient for reactant *i* in Eq. (7), and v_i'' is the stoichiometric coefficient for product *i*.

This finite-rate chemistry differs from the infinitely fast chemistry based on an equilibrium assumption in the previous studies of the BKD combustor [32,33,37–39]. Although a one-step reaction model would produce a higher flame temperature when carried out over a long time compared to an equilibrium chemistry model because of a lack of reverse reaction, the one-step reaction model takes into account the reaction time rather than assuming an infinitely fast reaction rate. Thus, it can capture the time delay between propellant injection and ignition, ensuring that combustion in the rocket engine initiates reliably and consistently when the fuel and oxidizer are mixed. The one-step chemistry model has been employed by Xiong et al. [41–43] to simulate nonlinear methane–oxygen combustion instabilities in multi-injector combustion chambers. It has also been verified by the authors using a two-dimensional reacting mixing layer in the previous work [58].

B. Numerical Solver

The governing equations in Sec. II.A are solved by an in-house code using the second-order cell-centered finite-volume method based on multiblock structured hexahedral grids. The code can simulate steady and unsteady compressible reacting turbulent flows with varying thermodynamic properties of each species and specified chemistry models. It has been verified by simulating the steady nonreacting and reacting flows in a two-dimensional mixing layer and a turbine cascade [58] and the unsteady reacting flow in a three-dimensional turbine stage [59]. In the present study, the convective and diffusive fluxes are discretized by the Jameson–Schmidt–Turkel (JST) scheme [60] and the second-order central scheme, respectively. In the species equation (1a) and energy equation (1c), the source terms exhibit fundamentally different physical properties from the convection and diffusion terms due to significantly smaller time scales for chemical reactions than for the flow, resulting in strong stiffness in solving the governing equations. A steady-state preserving operator splitting scheme was proposed to efficiently integrate the stiff governing equations in time for steady problems [58] and then extended to unsteady problems [59]. This extended splitting scheme is used

for time integration in this study. Parallel techniques based on message passing interface (MPI) are adopted to accelerate the computation by distributing grid blocks among CPU processors.

Structured hexahedral grids offer advantages in achieving high accuracy and great computational efficiency over unstructured tetrahedral or prismatic grids for the same grid number. For the configuration where multiple coaxial fuel and oxidizer injectors are discretely distributed at the entrance of a rocket combustion chamber, however, it is too complex to generate point-to-point connected structured grids at the interface due to different scales of injectors and chamber. Even if possible, the grid number and thus computational cost will be too huge to be acceptable. To overcome this, a patched grid, in which grids are separately generated for the injectors and chamber and then patched together by a non-point-to-point connected grid interface, is used in this study. On the patched-grid interface between the injectors and chamber, the volume-weighted interpolation method originally developed for data exchange across the interface between adjacent blade rows in turbomachinery [61–63] is extended and applied to interpolate flow variables. A cell that is not connected with any cells on the other side is treated as a wall boundary cell.

Consider the process to interpolate flow variables in the target hexahedral cell $\mathbf{ABCD}$ - $\mathbf{EFGH}$ from the source cells, which are connected with the quadrilateral ABCD on the interface, as shown in Fig. 1. The polygons produced by the intersection of the quadrilateral ABCD and the source quadrilaterals on the interface can be determined by the Sutherland–Hodgman algorithm [64]. The area ratio of the intersected polygon to the source quadrilateral, λ_i, is then computed for each source cell *i*. If the summation of areas of all intersected polygons is less than that of the quadrilateral ABCD, meaning that ABCD is not completely overlapped by the source quadrilaterals, contribution from the target cell itself should also be included. Assume that the ratio of the area difference to that of ABCD is λ_t. For the target cell itself and each source cell, the volume weight to interpolate the flow variables in cell $\mathbf{ABCD}$ - $\mathbf{EFGH}$ is expressed as

$$\varepsilon_t = \frac{\lambda_t \Omega_t}{\Omega}, \qquad \varepsilon_i = \frac{\lambda_i \Omega_i}{\Omega}, \qquad i = 1, 2, \ldots, n \tag{10}$$

where $\Omega = \lambda_t \Omega_t + \sum_{k=1}^{n} \lambda_k \Omega_k$, *n* is the number of source cells that intersect with $\mathbf{ABCD}$ - $\mathbf{EFGH}$, and Ω_t and Ω_i are the volumes of $\mathbf{ABCD}$ - $\mathbf{EFGH}$ and the *i*th source cell, respectively. The flow variable φ in $\mathbf{ABCD}$ - $\mathbf{EFGH}$ is then computed by

$$\varphi = \varphi_t \varepsilon_t + \sum_{i=1}^{n} \varphi_i \varepsilon_i \tag{11}$$

where φ_t and φ_i represent the flow variables in the target cell and in the *i*th source cell, respectively. The velocity in the target cell should be modified to its opposite value before being used in Eq. (11) to

maintain a no-slip wall. The interpolated flow variables in the target cell are then assigned to the corresponding ghost cell to set the interface boundary condition.

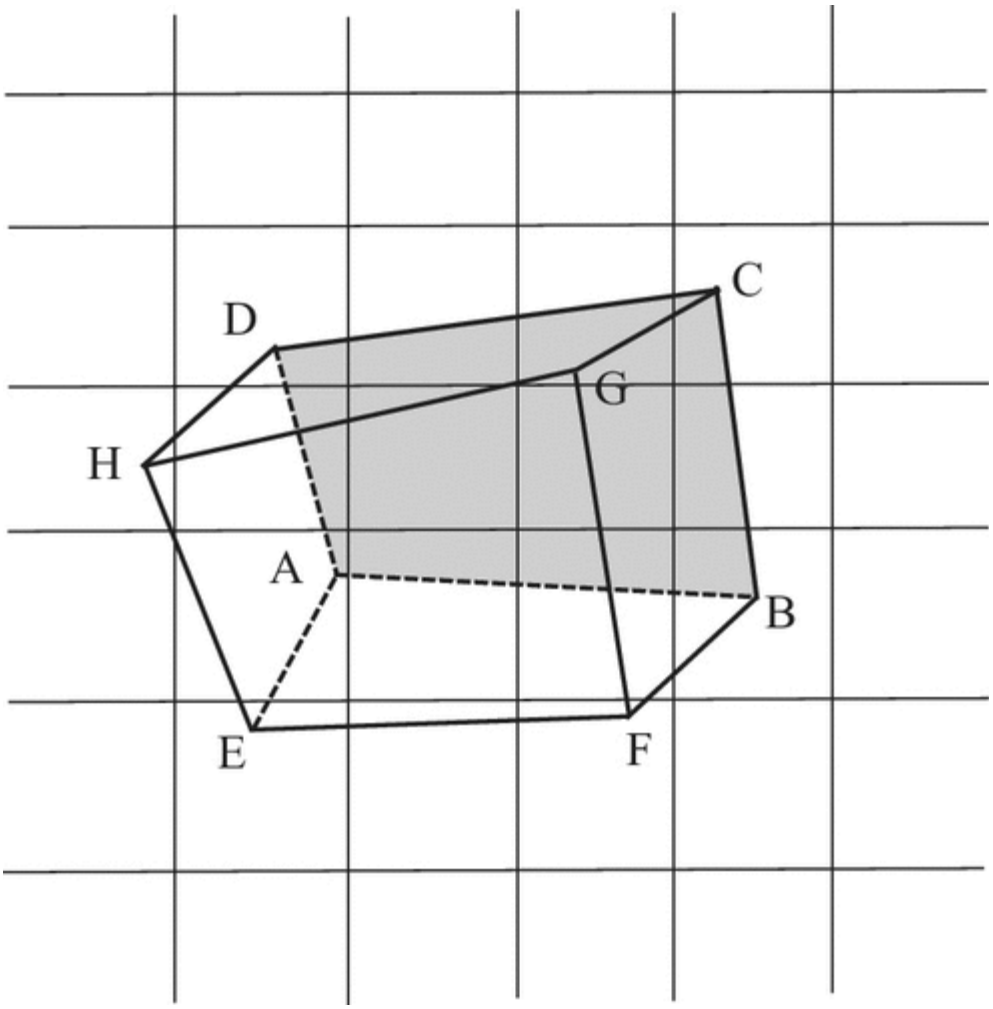

Fig. 1

Sketch of volume-weighted interpolation on the interface.

The area ratio of the target quadrilateral, λ_t, lies between 0 and 1. If the area summation of all intersected polygons is equal to that of the quadrilateral ABCD, i.e., $\lambda_t = 0$, then the above interpolation process degenerates into the original volume-weighted interpolation in Refs. [61–63]. On the other hand, if $\lambda_t = 1$, indicating that there are no intersected source cells found on the opposite side of the interface, i.e., $n = 0$, then only the first term in Eq. (11) is nonzero and $\varepsilon_t = 1$, resulting in a wall boundary cell.

Since for a second-order finite-volume method, flow variables defined at a cell center can also be treated as the volume-averaged values over the cell, the volume-weighted interpolation method can perfectly ensure the flow conservation across the interface. For cases in which the upstream and downstream domains are fully overlapping with each other on the interface, like the situations in multiblade-row turbomachines, numerical simulations based on the RANS equations show that the relative errors in the conservation of mass, momentum, energy, and other integrated quantities

across the interface consistently remain below 10^{-5} [61]. For the present rocket-engine case in which computational domains are not completely overlapping with each other on the interface, computations show that the relative error of mass flow rate across the interface is still less than 10^{-5} attributed to the fine mesh in LES. Attributed to the excellent flowfield continuity across the interface, the dynamics in the recess region are expected not to be affected by the patched grid.

C. Computational Configuration and Grid

The BKD rocket combustor, developed for studying self-excited high-frequency combustion instabilities at the German Aerospace Center (DLR) [26–31], is used in this study. The BKD engine, as shown in Fig. 2, consists of 42 coaxial injectors, a cylindrical combustion chamber of 80 mm diameter and 215 mm length, and a choked nozzle with a throat diameter of 50 mm. The injection head comprises three concentric rings of 6, 12, and 24 equidistant injectors, respectively, shown at the bottom left of Fig. 2. For each injector element, the oxidizer post has a diameter of 3.6 mm, while the fuel injector annulus has an inner diameter of 4 mm and an outer diameter of 4.5 mm. The two injectors are recessed by 2 mm at the chamber entrance. The oxidizer post is connected to the upstream dome through a throttle of 3.1 mm length, which is much shorter compared to the post length of 68 mm. Similarly, the fuel injector annulus, measuring 9.5 mm in length, is connected to an upstream annular section with a 28 mm length and a 7 mm outer diameter via a throttle. Different from the earlier studies [32,33,37,40], the present simulation simplifies the propellant injection system by omitting the domes, throttles, and the upstream fuel injector section. A close-up view of an individual injector is shown at the bottom right of Fig. 2. This simplification is made to reduce computational costs and to focus specifically on the flow within the oxidizer post, chamber, and exhaust nozzle. The computation by Urbano et al. [37] confirmed that there are no pressure fluctuations in the fuel injector and domes.

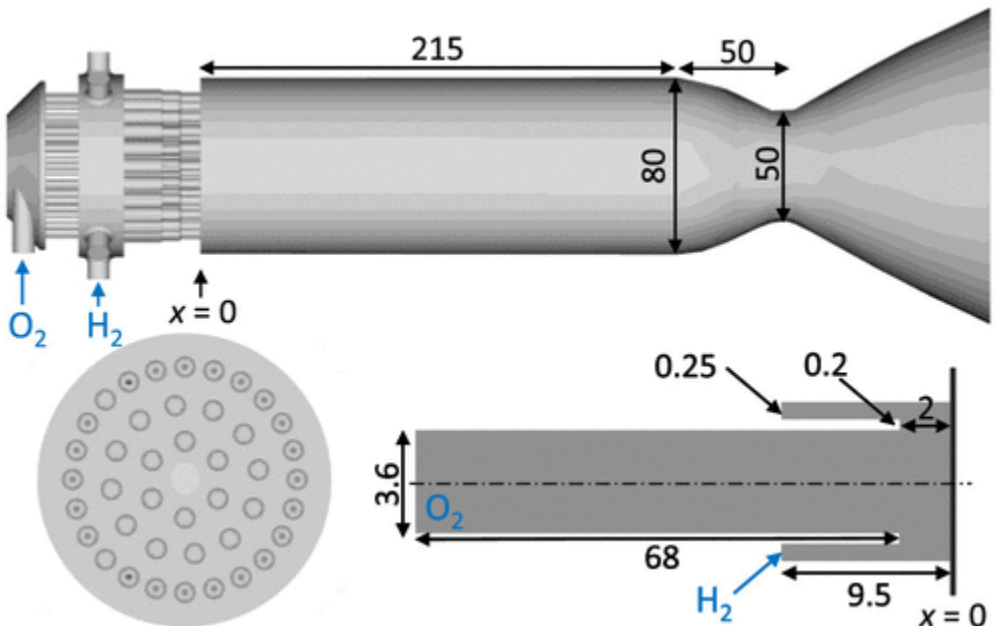

Fig. 2

Geometric configuration of BKD rocket combustor (units: mm).

In consideration of the circumferential periodicity of the chamber and injection system and the standing wave nature of the 1T mode in the chamber, multiblock structured hexahedral grids are generated for the half-cylinder of the rocket combustor, as shown in Fig. 3. Thus, the three-ring injection system reduces to 3, 6, and 12 injectors from inner to outer, respectively. Structured grids are separately generated for each injector and the chamber and then patched together at the chamber entrance. Each injector contains 0.14 million grid cells, while the chamber along with the nozzle consists of 14.94 million cells. This produces a total cell number of almost 18 million in the half-cylinder computational domain, and over 83% of the grid cells are placed in the chamber and nozzle. The dimensionless distance y^+ of the first grid point away from the wall is less than one for the chamber. However, there is more than one on the injector surfaces.

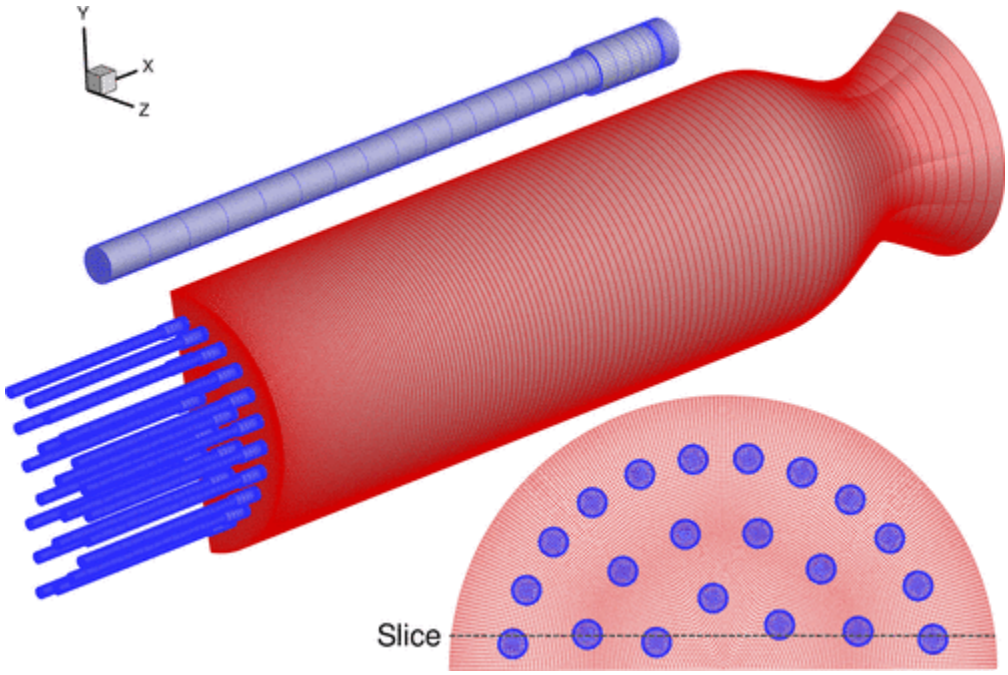

Fig. 3

Computational grid of BKD rocket combustor. Every other grid point is shown.

In this study, most grid points are concentrated in the combustion chamber, while relatively coarser grids are generated in injectors. This gridding strategy differs from the previous computations based on unstructured tetrahedral or prismatic grids [32,33,37,40]. Those studies prioritized high-resolution modeling of the propellant injection system, resulting in entire grids containing 55 million points [32], 174 million points [33], and 70 million elements [37,40] within the full-cylinder domain. By simplifying the rocket combustor configuration and employing structured grids, the total grid resolution for the half-cylinder domain is reduced to approximately half of the unstructured elements used in full-cylinder simulations that included the injection system [37,40]. Despite the reduction of the total number of grid points, our results demonstrate high resolution of the flow and flame structures in the combustion chamber and the coupled instability modes. As a reference, Xiong et al. [42] employed unstructured grids with a total of 12.1 million nodes to investigate the combustion

instability in a 30-injector rocket combustor featuring a simplified injection system similar to that in the present study.

The operating condition corresponding to an unstable load point, referred to as LP4 in the experiment, is numerically investigated in this study. In the experiment, the fuel injectors provide hydrogen with a mass flow rate of $0.96\ \mathrm{kg/s}$, temperature of 95.7 K, and pressure of 10.3 MPa, while the mass flow rate, temperature, and pressure of oxygen are $5.75\ \mathrm{kg/s}$, 111.4 K, and 9.4 MPa, respectively. The combustion is thus globally fuel-rich with an equivalence ratio of 0.75, producing an adiabatic flame temperature of 3910 K for complete combustion in the equilibrium state of constant pressure. Obviously, hydrogen is provided in a supercritical gaseous state at this load point, and oxygen is in a transcritical liquid state with a high density. To meet the temperature ranges ($200 \sim 6000\ \mathrm{K}$) of NASA polynomials for thermodynamic properties, the stagnation temperatures of hydrogen and oxygen at their injector inlets are adjusted to 210 K and 230 K in the present computation, respectively.

At the inlets of fuel and oxidizer injectors, the stagnation temperature and overall mass flow rate of gas are prescribed. During the computation, the axial momentum of each surface cell at the inlet is scaled to meet the prescribed overall mass flow rate. The turbulence intensity and ratio of turbulent to molecular viscosity are set as 10% and 10.0 at the inlet, respectively. They are used to synthesize realistic turbulent fluctuation conditions at the inlet by the random flow generation (RFG) method proposed by Smirnov et al. [65]. All flow quantities are extrapolated at the exit of the nozzle since the flow is supersonic there. This ensures that no waves propagate backward into the computational domain at the exit. The symmetry plane of the chamber is treated as a slip-reflected wall, which will produce standing tangential modes in the chamber, and crossflow and diffusion at this plane are dismissed. Since the symmetry plane is a pressure antinode attributed to the nature of the standing tangential mode in this combustor, velocity fluctuations and normal velocity on the plane are expected to be negligible. All side surfaces are specified as adiabatic walls with zero normal pressure gradient. No-slip boundary conditions are imposed on the surfaces of the combustion chamber and nozzle, while slip is allocated on the injector surfaces. The present study focuses on the longitudinal acoustic behavior of the flow within injectors, which is minimally influenced by sidewall skin friction. Consequently, modeling injector surfaces with slip-wall boundary conditions introduces negligible uncertainty in simulating longitudinal acoustic waves. Although the injector walls are treated as slip surfaces, the effect of viscous dissipation is still incorporated into the injector flow dynamics by wave-created gradients.

Carefully constructed initial conditions are used to enhance ignition and quickly establish the operating condition. A third circumferential domain (60° sector) of the whole computational grid is first computed as a guided case. At the initial stage, the chamber is filled with water vapor with a temperature of 1500 K, while the fuel and oxidizer injectors are hydrogen and oxygen at 200 K temperature, respectively. Since no explicit ignition model is included in the current simulation, the hot product ensures that the cold fuel and oxidizer can quickly ignite when they mix in the chamber. The time that the reactants are earliest injected into the chamber and transported outside the nozzle

exit is about 0.7 ms. After 2 ms, the solution in the $60°$ sector is transferred to the half-cylinder domain by repeating it twice in the circumferential direction. The computational time in the half-cylinder domain is over 4 ms, and the time interval Δt to output flowfields is 0.002 ms. The flow integration time step is determined by the minimum allowable value across all grid cells and is on the order of 5.0×10^{-9} s. The computational cost is about 30,000 CPU hours per millisecond of physical time on 384 AMD EPYC 7H12 Rome cores.

D. Dynamic Mode Decomposition

In the analysis of combustion instability, fast Fourier transform (FFT) is usually applied to a time series to obtain the dominant frequencies and their individual amplitudes. However, the dynamic mode decomposition (DMD) [66,67] approach can give not only the mode shapes of a time series of fields and their frequencies but also the growth rates of modes. The basic mathematical process of DMD is shortly introduced here.

The $n+1$ snapshots of an unsteady flowfield with a dimension of m are collected into two matrices: $\boldsymbol{W}_1^n = \{\boldsymbol{w}_1, \boldsymbol{w}_2, \dots, \boldsymbol{w}_n\} \in \mathbb{R}^{m\times n}$ and $\boldsymbol{W}_2^{n+1} = \{\boldsymbol{w}_2, \boldsymbol{w}_3, \dots, \boldsymbol{w}_{n+1}\} \in \mathbb{R}^{m\times n}$, where $\boldsymbol{w}_k \in \mathbb{R}^m$ is the kth snapshot vector, and $m \gg n$. DMD assumes that two successive snapshots satisfy a linear relation,

$$\boldsymbol{W}_2^{n+1} = \boldsymbol{A}\boldsymbol{W}_1^n \tag{12}$$

where the unknown matrix $\boldsymbol{A} \in \mathbb{R}^{m\times m}$ is a linear approximation to the dynamic evolution of a nonlinear flow system. The singular value decomposition of the matrix $\boldsymbol{W}_1^n$ is

$$\boldsymbol{W}_1^n = \boldsymbol{U}\boldsymbol{\Sigma}\boldsymbol{V}^T \tag{13}$$

Substituting the above equation into Eq. (12) gives

$$\boldsymbol{U}^T\boldsymbol{A}\boldsymbol{U} = \tilde{\boldsymbol{A}}, \quad \tilde{\boldsymbol{A}} = \boldsymbol{U}^T\boldsymbol{W}_2^{n+1}\boldsymbol{V}\boldsymbol{\Sigma}^{-1} \tag{14}$$

The eigenvalues, $\lambda_k \in \mathbb{C}$, and eigenvectors, $\boldsymbol{y}_k \in \mathbb{C}^n$, of the matrix $\tilde{\boldsymbol{A}} \in \mathbb{R}^{n\times n}$, which are easy to be determined attributed to its low dimension, are a subset of those of $\boldsymbol{A}$. The kth eigenvalue (DMD eigenvalue) of $\boldsymbol{A}$ is also λ_k, and the corresponding eigenvector (DMD mode shape) is

$$\boldsymbol{\phi}_k = \boldsymbol{U}\boldsymbol{y}_k \tag{15}$$

The complex growth rate of the *k*th DMD mode is

$$\mu_k = \frac{\ell n \lambda_k}{\Delta t} \tag{16}$$

where Δt is the time interval between two successive snapshots. The real part and imaginary part of μ_k are the temporal growth rate and angular frequency of the *k*th DMD mode, respectively.

III. Results and Discussion

A. Averaged Results

Figure 4 shows the history of the stagnation temperature and pressure averaged over the chamber. Since the solution in the 60° sector domain is used as the initial condition for the computation in the half-cylinder, a quasi-steady state is quickly established in the chamber after about 1.6 ms. In the quasi-steady regime, the averaged stagnation temperature and pressure are 3500 K and 80 bar, respectively, and the peak-to-peak oscillation amplitudes are 70 K and 5 bar, respectively. The time that gases pass through the chamber is estimated to be 0.7 ms. Hence, the flowfields between 1.6 and 3.6 ms, corresponding to three flow passing periods, are chosen to analyze the combustion instability in the rocket combustor in this study unless otherwise stated.

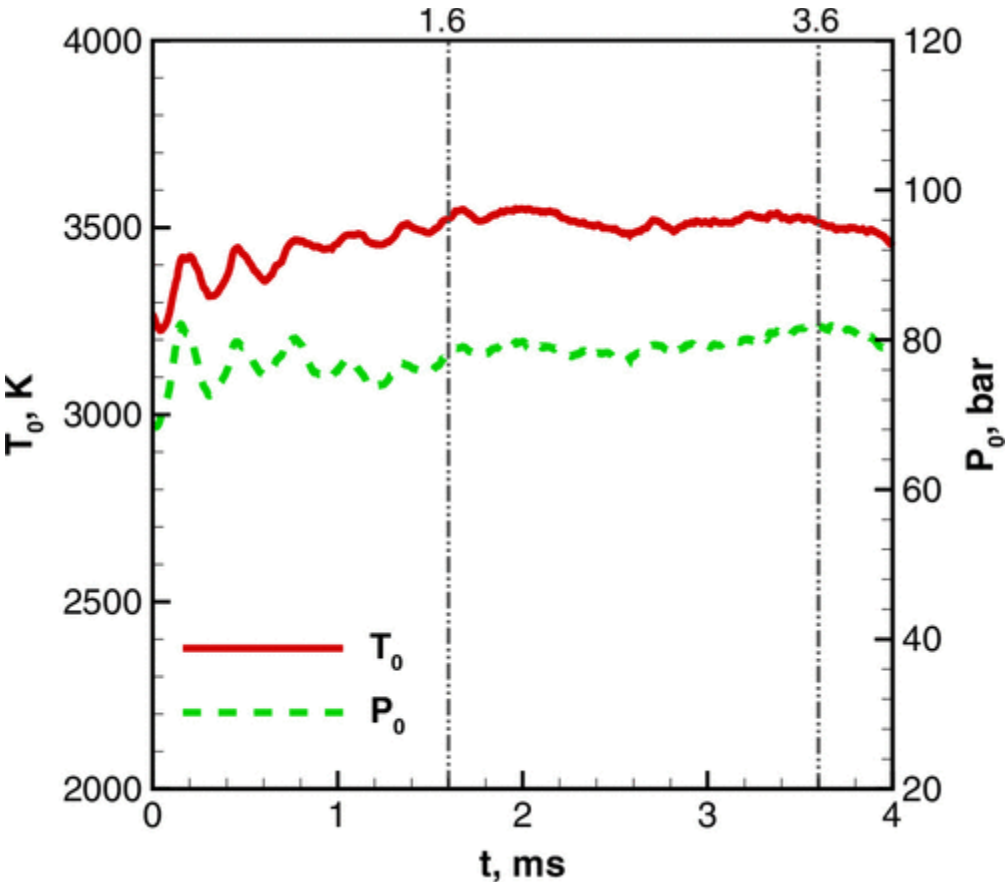

Fig. 4

History of stagnation temperature and pressure averaged over chamber.

For the time-averaged flow, Fig. 5 shows the axial variations of cross-section-averaged stagnation temperature, stagnation pressure, and mass fractions of each species. Near the injector exits ($x < 10$ mm, corresponding to 2 injector diameters), the stagnation pressure drops rapidly due to the strong mixing between fuel and oxidizer jets as well as the recirculation flows between the jets and the front plate of the chamber. After that, the stagnation pressure reduces slowly, attributed to the chemical reaction, turbulent diffusion, and skin friction of the side wall. Chemical reaction mainly happens in the early part of the chamber, as indicated by the quick changes of stagnation temperature and mass fractions. Specifically, 80% oxygen from upstream injectors has been consumed at $x = 50$ mm, corresponding to 11 injector diameters or a quarter of the chamber length. At $x = 150$ mm, two-thirds of the chamber length, almost all hydrogen has been burned.

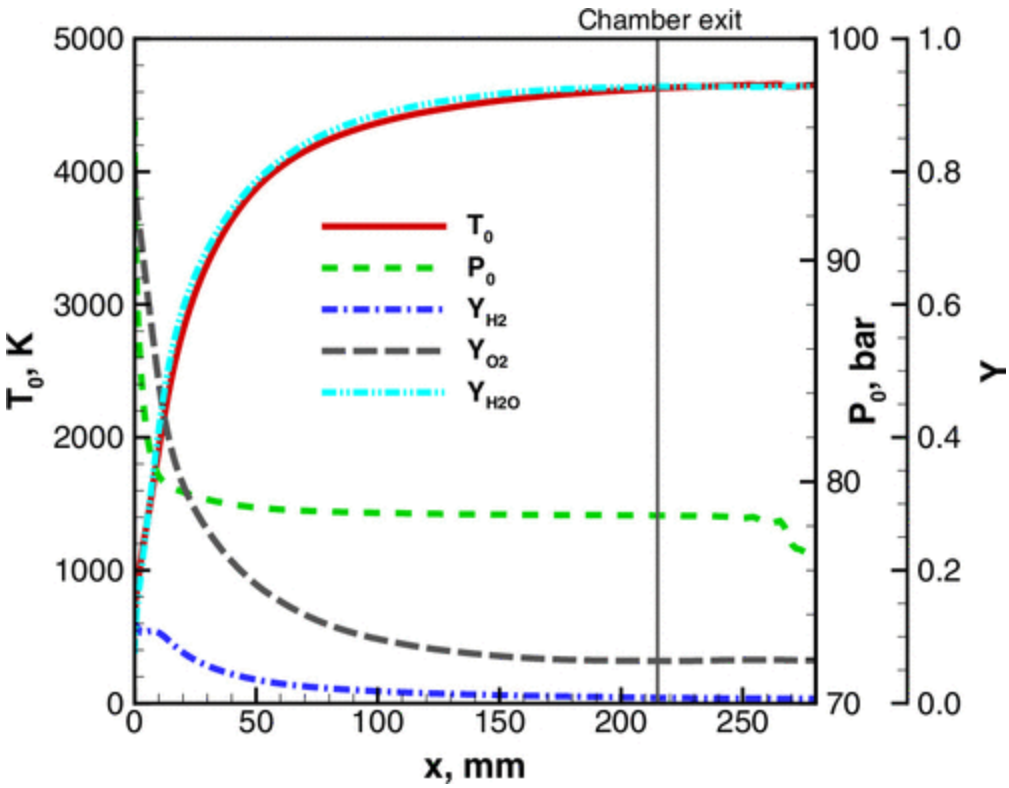

Fig. 5

Axial variations of cross-section-averaged stagnation temperature, stagnation pressure, and mass fractions.

To further verify the present simulation, Table 1 compares the mean stagnation pressure and temperature in the combustion chamber with the experimental data and other computational results from Ref. [34]. The computed pressure is closely matched by all simulations and slightly lower than the measured value. Specifically, the relative difference of pressure between the present computation and the experiment is 1.6%. The present chamber temperature is 300 K higher than that by the Institut de Mécanique des Fluides de Toulouse (IMFT) [37]. This discrepancy is attributed to two causes. One is that the temperature of injected hydrogen and oxygen is about 120 K higher than that in the experiment and by IMFT, and a perfect gas is assumed in this study instead of a real-gas model as used by IMFT. The other is that the global reaction mechanism without reverse reactions is employed as the chemistry model in this study, resulting in faster combustion in the chamber. Some unburnt gases reach the nozzle, as indicated by the nonzero mass fractions of oxygen and hydrogen at the chamber exit. This incomplete combustion in the chamber is consistent with the simulation by IMFT [37].

Figure 6 shows the contours of time-averaged temperature, axial velocity, and flame index on a longitudinal slice. The slice is parallel to the symmetry plane of the computational domain and passes through six injectors, as shown in Fig. 3. The flame index (FI) is defined as the heat release rate per unit volume masked by the sign of the dot product of the gradients of fuel and oxidizer mass fractions, i.e.,

$$\mathrm{FI} = \mathrm{sign}(\nabla Y_{\mathrm{H_2}} \cdot \nabla Y_{\mathrm{O_2}}) \cdot \dot{Q} \tag{17}$$

where the heat release rate is computed by Eq. (5). If the flame index is positive, fuel and oxidizer diffuse in the same direction, indicating a premixed flame; otherwise, it means a diffusion flame. Since the diffusion and mixing characteristics of the gaseous propellants differ from those of the liquid oxygen used in the experiment, the flame index in this simulation may deviate from that in the actual engine, particularly near the chamber entrance. In the downstream combustor, however, the gradient signs of the propellants in the simulation are expected to be more realistic, as the liquid oxygen is assumed to vaporize rapidly. Due to the high reactivity of hydrogen, a diffusion flame is established right at the recess region of an injector. For each injector, the oxygen is injected into the chamber as a round jet, while the hydrogen forms an annular jet outside the oxygen jet. There is a rapid expansion of hydrogen and oxygen near the chamber entrance, as shown by the low temperature there. Recirculation happens between adjacent jets and in the chamber wall corners, indicated by the negative axial velocity. In these recirculation regions, combustion is controlled by premixed flames. This differs from the experimental observations by Armbruster et al. [29], where no flame was detected in the recirculation regions based on OH^* imaging. The discrepancy may be attributed to the rapid chemical reactions resulting from the high injection temperature and the omission of propellant vaporization in the simulation. The jet expansion length, recirculation region size, and premixed flame size are all approximately 10 mm, which is consistent with the axial range where the stagnation pressure drops rapidly in Fig. 5. As the combustion develops along the axial direction, the temperature rises quickly and then approaches uniformity in the cross-section plane. The velocity also increases along the axial direction since the heat released by the chemical reaction is converted into kinetic energy. In the whole chamber, the combustion is dominated by diffusion flames except in the recirculation regions and several downstream streak regions where premixed flames are found.

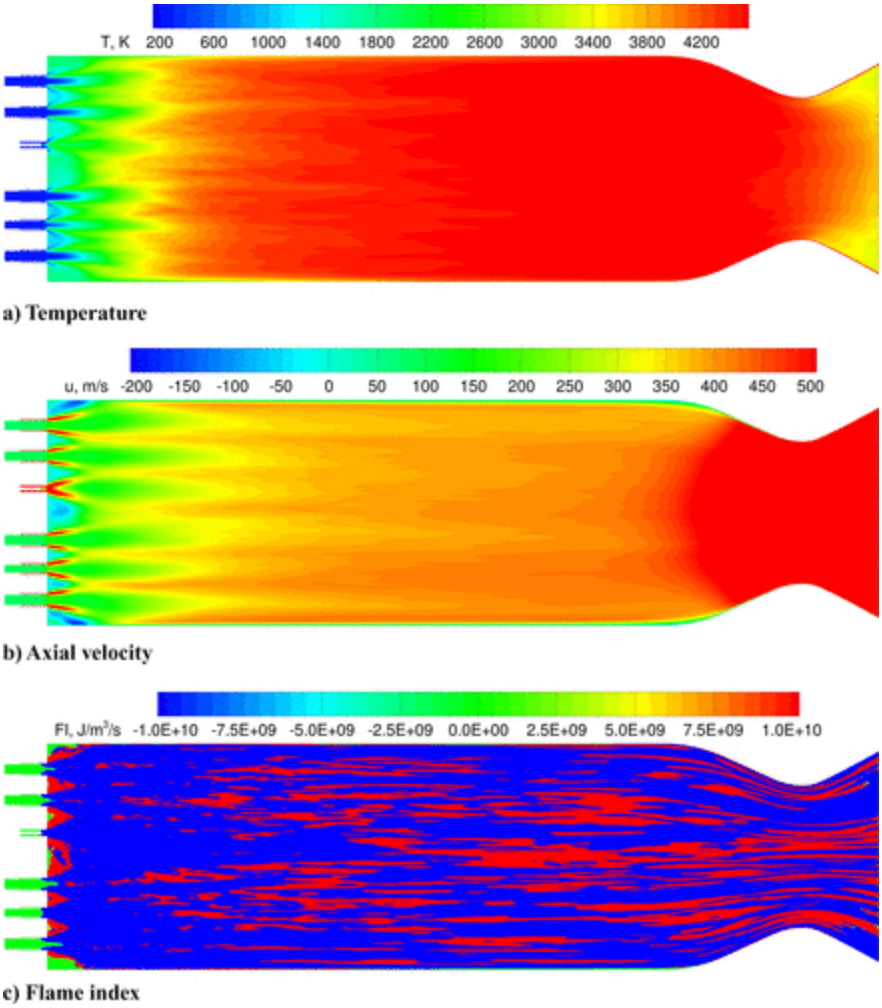

Fig. 6

Time-averaged contours on longitudinal slice.

B. Unsteady Results

To demonstrate the present LES computation captures the turbulent features, the spectral energy at two arbitrarily selected points on the chamber centerline is obtained by performing FFT on the velocity and shown in Fig. 7. The spectral energy of velocity follows the $-5/3$ law in high-frequency ranges. This partially indicates that the LES computation based on the current mesh captures turbulent fluctuation features in the combustion chamber.

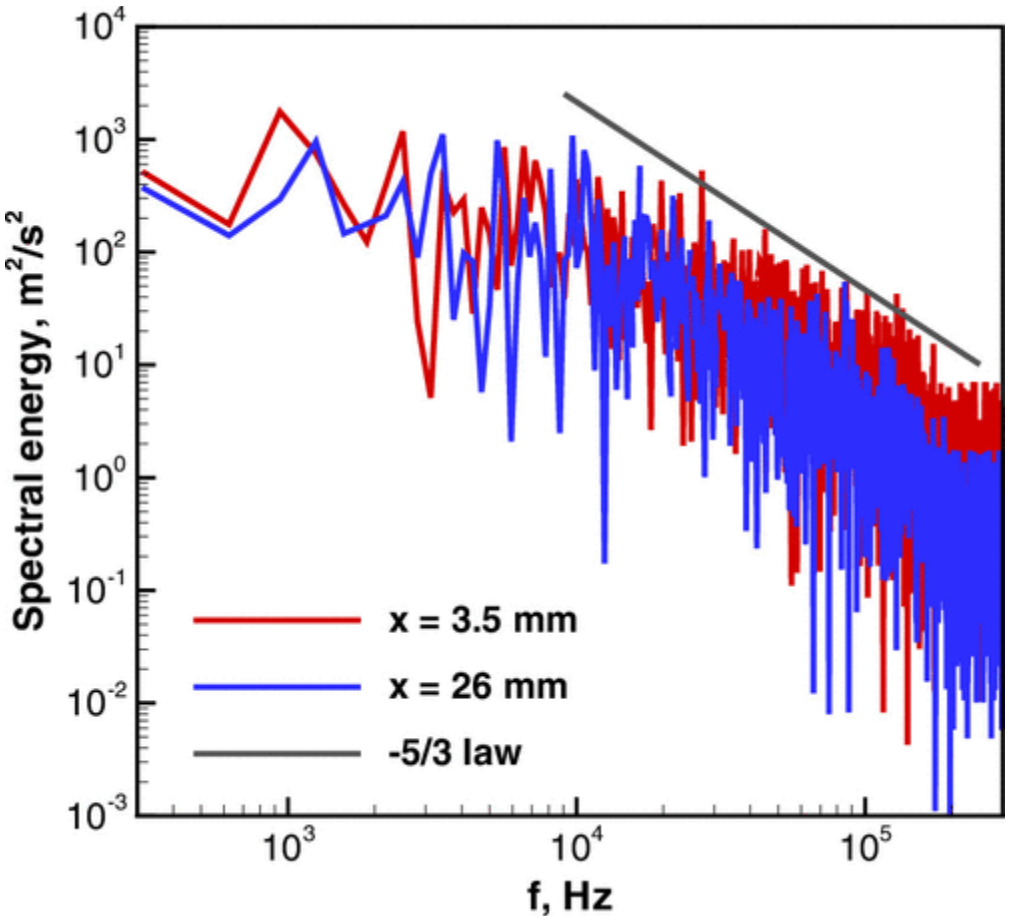

Fig. 7

Spectral energy at two points on chamber centerline.

Figure 8 shows the instantaneous contours of temperature, axial velocity, and flame index on the longitudinal slice, the same as that in Fig. 6. In the combustion chamber, the shear layers among the fuel jet, oxidizer jet, and primary flow become unstable after about two injector diameters due to the Kelvin–Helmholtz instability induced by high velocity differences. This axial position corresponds to the time-averaged expansion length of propellant jets as shown in Fig. 6. Many circumferential vortices are then generated, enlarged, and transported downstream. After a quarter of the chamber length, the temperature is high enough and almost uniform in the cross-section plane, except for several low-temperature spots. This is consistent with the axial range in which the combustion is almost completed in the time-average sense, as shown in Fig. 5. However, the velocity remains nonuniform in the whole chamber due to the influence of low-speed oxygen transported from upstream. This indicates that the heat diffusion in the chamber is stronger than the momentum diffusion. Flames are established within the shear layers between hydrogen and oxygen, as indicated by the regions with a high flame index. Premixed flames dominate near the injectors, while they switch to diffusion flames in the downstream region. This phenomenon was also observed in rocket combustors using methane as fuel by Xiong et al. [42,43] and Zhan et al. [44]. Few flames even reach to the downstream exhaust nozzle.

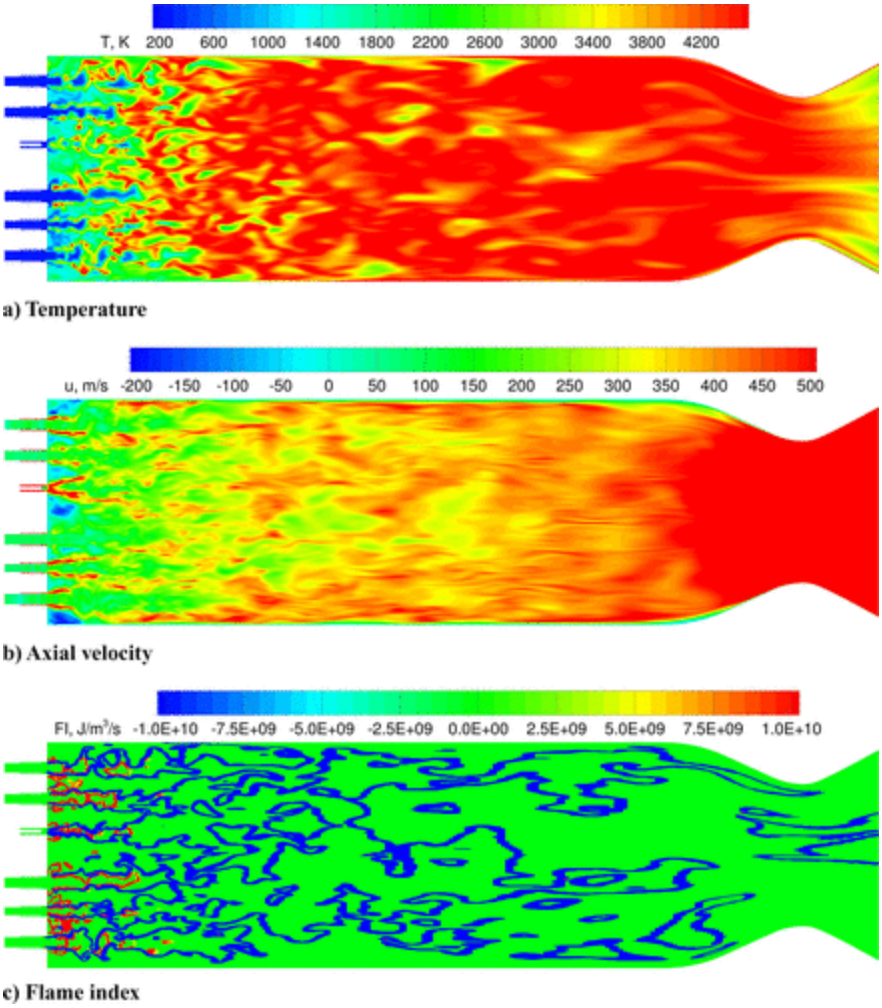

Fig. 8

Instantaneous contours on longitudinal slice.

To confirm that the acoustic instabilities happen in the combustion chamber, the history of the static pressure at two probing points on the chamber wall at $x = 5.5 \ \ \mathrm{mm}$ is shown in Fig. 9. The pressure at the two points varies in a similar way since both of them are on the symmetry plane of the domain and satisfy the same boundary condition. The pressure oscillates with a high amplitude and high frequency starting from the computation and reaches a limit cycle after 1.5 ms. At several individual time instants, the pressure exceeds 100 bar, and at one particular moment, it reaches as high as 160 bar—twice the mean chamber pressure. In the limit cycle regime, the root-mean-square value of pressure fluctuation in 2 ms is around 4 bar, i.e., 5% of the mean chamber pressure. All these indicate that acoustic instabilities arise in the chamber. Figure 10 shows the amplitude spectrum of the pressure at the two points obtained by performing FFT for the time series from 1.6 to 3.6 ms. Certain resonant frequencies are identified from the spectrum and labeled as 1L, 2L, 3L, 1T, 2T, and 1R. They correspond to the primary acoustic eigenvalues in the chamber, whose spatial structures are discussed in Sec. III.C. Among them, the 1T and 1L modes exhibit larger amplitudes than the others. Besides the marked ones, the other local peak frequencies in Fig. 10 are expected to be introduced by the pressure fluctuations from the upstream injectors since the two probed points are very close to the chamber entrance.

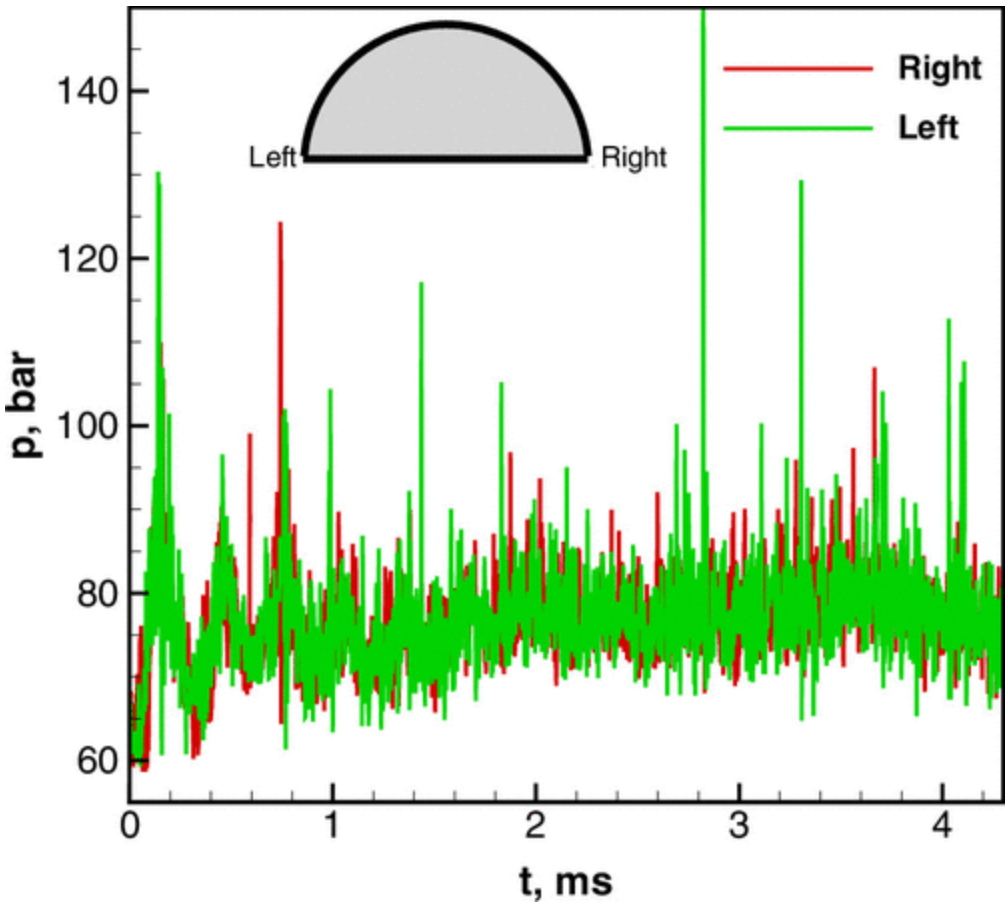

Fig. 9

History of pressure at $x = 5.5 \ \mathrm{mm}$ on chamber wall.

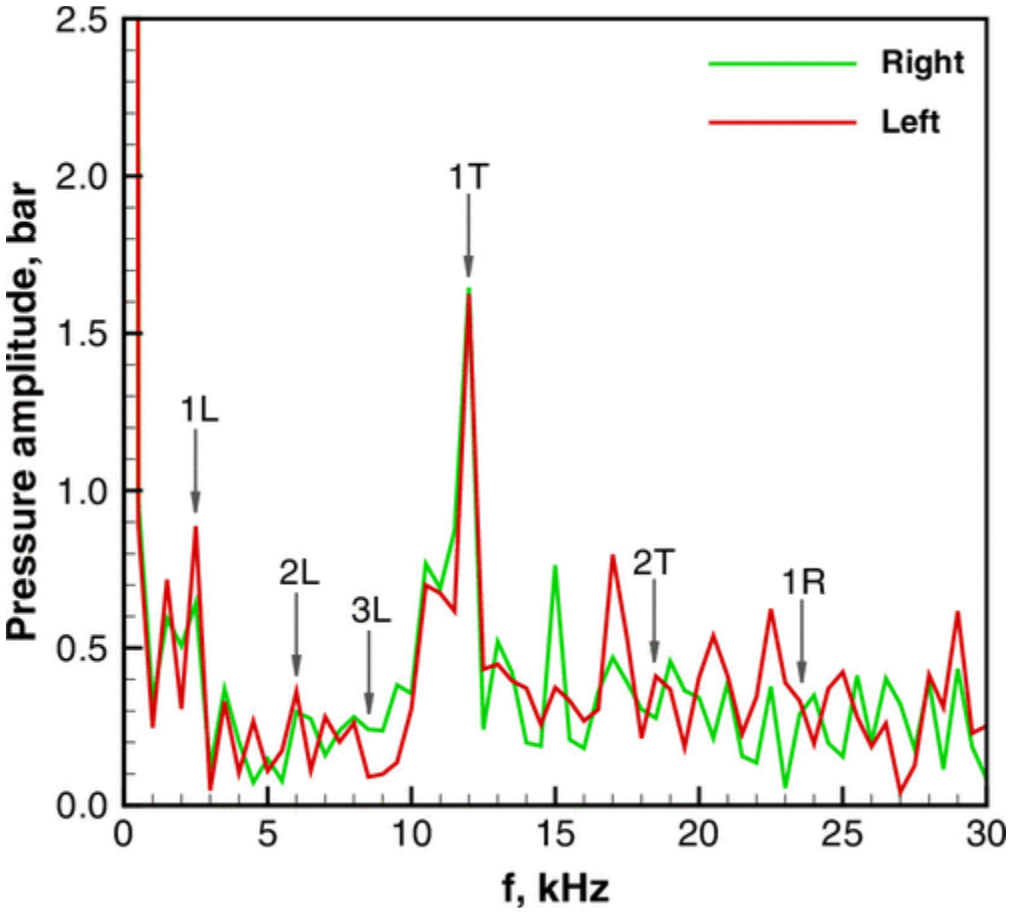

Fig. 10

Amplitude spectrum of pressure at $x = 5.5$ mm on chamber wall from 1.6 to 3.6 ms.

Table 2 compares the primary acoustic frequencies in the combustion chamber with the computational results by Urbano et al. [37] and the experimental data. FFT and DMD are applied to identify the acoustic modes in the chamber in the present study. Note that the frequency resolution (the frequency interval, not the cutoff frequency) in the FFT is 500 Hz, attributed to the time duration of 2 ms. The mode shapes at 2.5 and 3.0 kHz, two successive FFT frequencies, closely resemble the 1L mode and have comparable amplitudes. This indicates that both frequencies carry energy associated with the 1L mode. Consequently, the 1L mode frequency is determined as the average of these two frequencies, and the corresponding mode shape is obtained by summing their individual contributions. The same situation happens on the 1T mode by FFT. The frequencies of DMD modes are not restricted by the time duration but decided by the eigendecomposition of the snapshot series.

Although the physical backgrounds and mathematical processes of FFT and DMD are different, they obtain almost the same acoustic frequencies. The relative differences between them are less than 5% for all acoustic modes listed in Table 2 except for the 1T mode, which exceeds 6%. The frequencies of 1L and 2L modes in the present computation match well with the experimental data, with a difference less than 5%. Compared to the experiment and the computation by Urbano et al. [37], the present computation obtains higher frequencies for the high-order modes, especially for the 1R mode. The discrepancy is attributed to a cold zone near the chamber entrance, where relatively cold propellants

are injected and must undergo vaporization, atomization, mixing, and combustion before reaching chemical equilibrium [68]. This process reduces the effective speed of sound in both the first half and the full length of the chamber. Since transverse modes, including tangential and radial modes, predominantly reside in the upstream half of the chamber, as will be shown in Sec. III.C, they are more strongly influenced by the cold zone near the chamber entrance. In the present simulation, however, a higher injection temperature and the neglect of vaporization result in a higher temperature and thus speed of sound in the upstream region. As a result, the predicted acoustic frequencies, particularly for tangential and radial modes, are higher. Even so, the differences of both 1T and 1R mode frequencies are less than 10% between the present computation and Urbano et al. [37], and the differences between the present computation and experiment are less than 15% for the 1T, 2T, and 1R modes. Although the experiment detected the 3T mode frequency in the chamber, this wave shape and thus frequency are not clearly identified by either FFT or DMD in the present study. It was not reported by Urbano et al. [37], either.

Besides the frequency, the DMD approach also gives the growth rate of each mode. In this case, DMD reveals that all modes listed in Table 2 are damped. Interesting is that the immediate left and right modes of the 1T mode, which have the mode shapes extremely close to the 1T mode, have positive growth rates. In consideration of the sensitivity of growth rate to the data set in DMD in theory, this implies that energy transfer happens among acoustic modes close to the 1T mode, which might make the 1T mode unstable.

To examine the instabilities of acoustic waves, the dynamic features of the pressure in the chamber are further investigated by using FFT. Figure 11 shows the amplitude spectrum of the pressure at $x = 5.5\ \ \mathrm{mm}$ on the chamber wall in different time durations. The two selected points are the same as those in Fig. 10. As the flow develops with time, the amplitude of the 1T mode grows while that of the 1L mode decays. After 1.2 ms, the 1T mode exceeds the 1L mode and dominates the frequency spectrum. The present computation does not introduce any triggering perturbations into the chamber or injectors. Hence, we confirm that the present computation exhibits a self-excited first tangential combustion instability in the chamber.

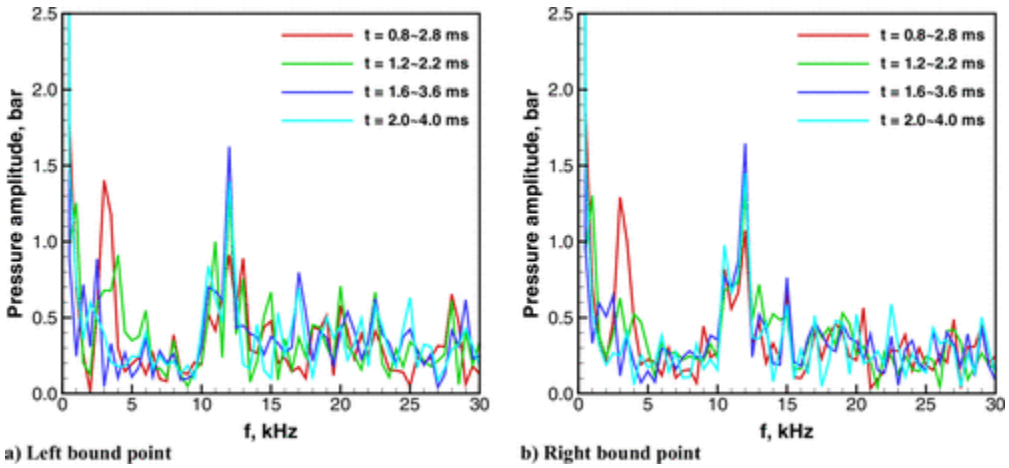

Fig. 11

Amplitude spectrum of pressure at $x = 5.5$ mm on chamber wall in different time durations.

The LES by Urbano et al. [37,38] found that the combustor is stable if no perturbation is imposed, while transverse instabilities are triggered by superimposing a large-amplitude (over 10% mean chamber pressure) 1T mode pressure disturbance onto the initial flowfield. The experiment by Gröning et al. [27] revealed that at this load point, the combustor is stable at low hydrogen temperatures while exhibiting a spontaneous 1T instability at a high temperature of around 100 K or above. Schmitt et al. [32,33] performed LES for different hydrogen injection temperatures (57, 65, and 131 K) and found that the 1T mode in the combustion chamber remains stable at the two lower injection temperatures but becomes naturally unstable at the highest temperature. In the present simulation, hydrogen is injected at a temperature of 210 K, which is high enough. This explains why the self-excited 1T instability is observed in the present computation.

C. Acoustic Mode Shapes

The spatial structures of the pressure fluctuation associated with the primary frequencies identified in Table 2 are examined and compared between FFT and DMD in this section. To focus on the combustion and avoid the distortion from upstream injectors, FFT and DMD are only performed for the unsteady pressure fields in the chamber and exhaust nozzle. Furthermore, to reduce the computational costs, the flowfields of 1000 snapshots on every other grid point are used. This produces over 2 million grid points for each snapshot. The mode shape is defined as the modulus of the real and imaginary parts at a specific frequency of FFT or DMD. An FFT mode shape value represents the absolute oscillation amplitude at each spatial location, whereas a DMD mode shape only provides the relative magnitude between locations.

The three longitudinal modes in the chamber are first analyzed. Since a longitudinal acoustic mode shape is expected to be uniform in the transverse plane, here we only examine the axial variation. Figure 12 shows the variations of 1L, 2L, and 3L mode shapes along the chamber centerline. Both FFT and DMD capture the sinusoidal shapes of longitudinal modes, i.e., 2, 3, and 4 antinodes for the 1L, 2L, and 3L modes, respectively. The amplitude of the pressure fluctuation has no zero point (node), indicating that the longitudinal mode in the chamber is not a simple superimposition of two opposite sinusoidal traveling waves. This is different from the solution to a linear wave equation in a close-ended pipe. This may be attributed to the nonlinearity of the Navier–Stokes equations solved in this study and the imperfect end-wall boundaries resulting from the injectors at the chamber entrance and the nozzle passage at the exit. Since the chamber exit is not an end wall but connected with a convergent-divergent nozzle, both pressure and velocity waves may be transmitted downstream. Therefore, the end of the chamber is not fixed as either a node or antinode. Note that the chamber length is 215 mm and the nozzle throat is 50 mm after the chamber exit. Figure 12 states that the rightmost antinodes always stay between the chamber exit and the nozzle throat as expected. As the mode order increases, the antinode gradually moves downstream. The pressure amplitude exhibits a strong oscillation in the region between the injector plate and $x = 50$ mm (11 injector diameters), implying strongly nonuniform jets and fast-developing combustion there.

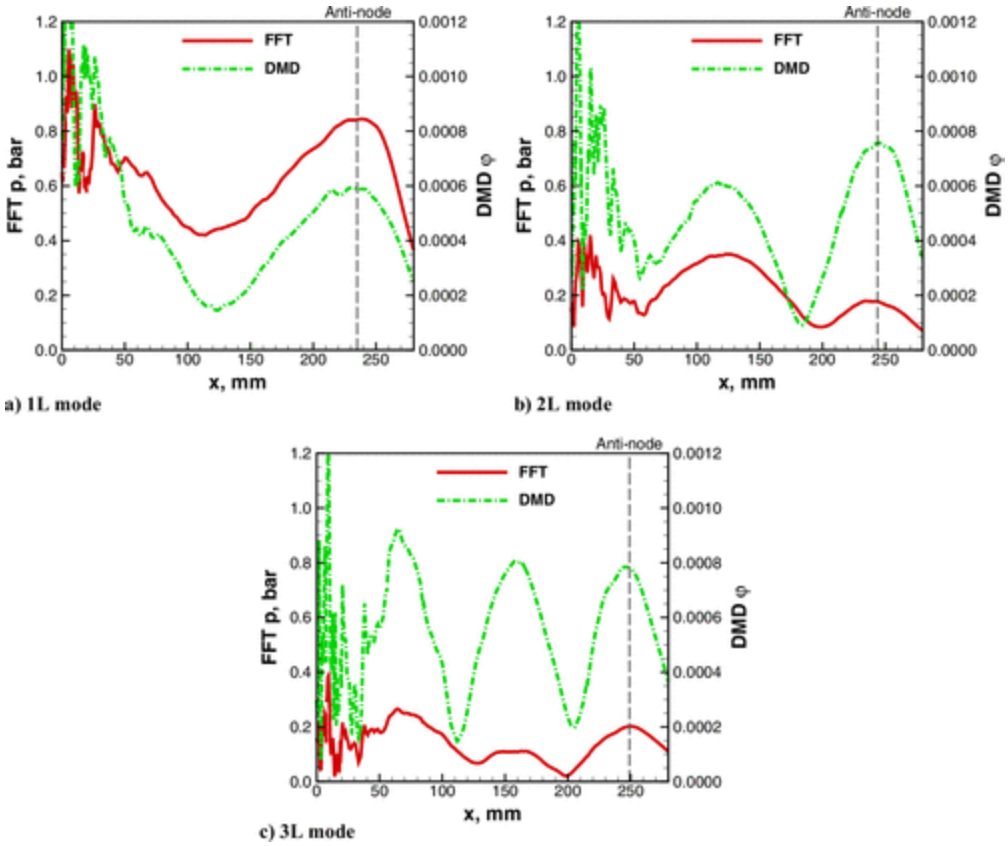

Fig. 12

Variation of longitudinal mode shape along chamber centerline.

In Fig. 12, all three longitudinal mode shapes decay along the axial direction as indicated by the attenuated pressure amplitudes at antinodes. This can be explained by the axial variation of the speed of sound in the chamber. If we ignore the influence of unsteady heat release rate, the pressure amplitude $\hat{p}$ of a harmonic with an angular frequency of ω is described by the homogeneous Helmholtz equation in the frequency domain:

$$\nabla \cdot [\bar{c}^2(\boldsymbol{x})\nabla\hat{p}(\boldsymbol{x})] + \omega^2\hat{p}(\boldsymbol{x}) = 0 \tag{18}$$

where $\bar{c}(\boldsymbol{x})$ is the time-averaged speed of sound, and $\boldsymbol{x}$ is the spatial coordinate. If we only consider the variation of $\hat{p}$ along the x direction for simplicity and further assume that $\bar{c}$ varies linearly with x, i.e., $\bar{c} = ax + b$, then Eq. (18) is reduced to

$$\bar{c}^2\frac{\mathrm{d}^2\hat{p}}{\mathrm{d}x^2} + 2a\bar{c}\frac{\mathrm{d}\hat{p}}{\mathrm{d}x} + \omega^2\hat{p} = 0 \tag{19}$$

By fixing $\bar{c}$ at x, the solution to the above equation in the neighborhood of x is

$$\widehat{p} = A\exp(-ax/\bar{c})\cos(kx) \tag{20}$$

where $k = \sqrt{\omega^2 - a^2}/\bar{c}$. Equation (20) indicates that the local pressure amplitude depends on the change rate of the speed of sound, *a*. If $a > 0$, the pressure amplitude damps along the *x* direction. Figure 13 shows the axial variations of cross-section-averaged speed of sound, static temperature, and gas constant. The temperature increases along the axial direction due to the heat released by chemical reaction, while the gas constant decreases due to the consumption of light hydrogen. The combined action of them leads to a parabolic variation of the speed of sound in the axial direction, with a peak in the middle of the chamber. According to Eq. (20), the pressure amplitude first rapidly decays and then gradually grows in the axial direction since the slope of the speed of sound, *a*, is strongly positive in the first half of the chamber and slightly negative in the latter half. This explains why the amplitude of a longitudinal mode at the chamber exit is smaller than that at the entrance.

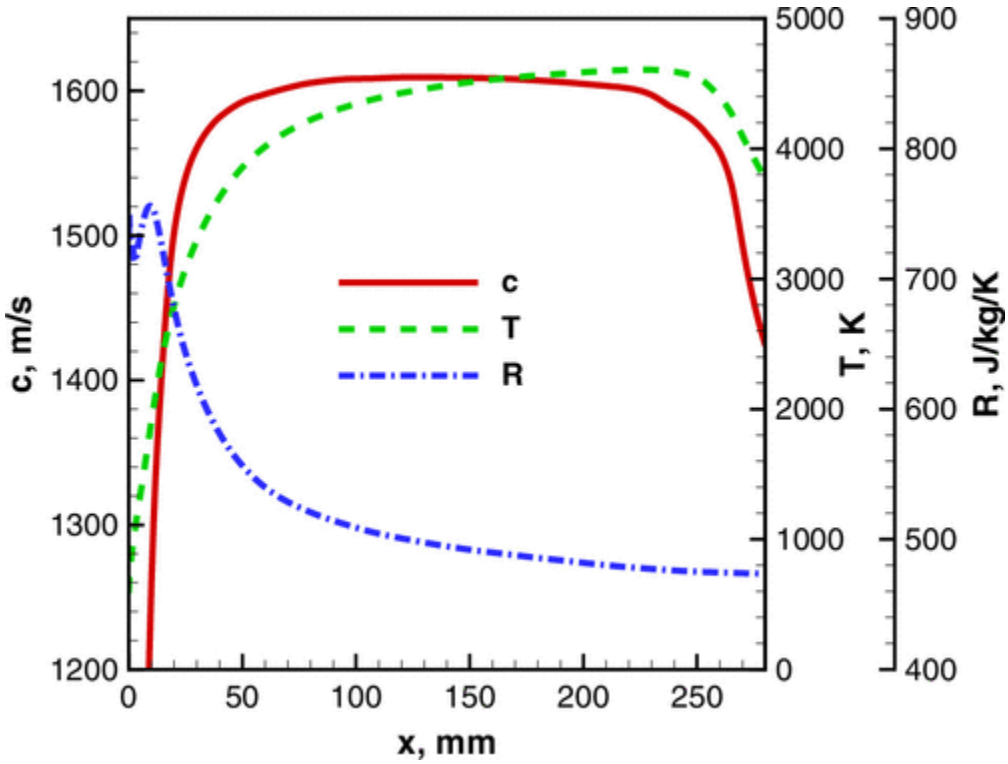

Fig. 13

Axial variations of cross-section-averaged speed of sound, static temperature, and gas constant.

The two tangential modes in the chamber are then examined. Figures 14 and 15 show the contours of the 1T and 2T mode shapes in the chamber, respectively. In each figure, the right part is the cylindrical wall surface, while the left part is a transverse slice at $x = 30\ \ \mathrm{mm}$. Both FFT and DMD successfully predict the ideal mode shape of the Helmholtz equation in a cylindrical coordinate system, i.e., the first-order Bessel function in the radial direction coupled with a first-order cosine wave in the azimuthal direction for the 1T mode, and the second-order Bessel function coupled with a second-

order cosine wave for the 2T mode. Along the axial direction, the pressure amplitudes of both 1T and 2T modes first decrease from a peak value and then increase to achieve a second smaller peak near the chamber exit. This is again attributed to the variation of the speed of sound along the axial direction, as discussed for the case of longitudinal modes in Fig. 12. This is slightly different from the results by Urbano et al. [37], in which the 1T mode quickly decays starting from the chamber entrance and the second peak does not appear downstream. This is because the global reaction mechanism without reverse reactions and the high injection temperature in the present simulation induce a fast consumption of hydrogen in the chamber, which results in a reduction of the gas constant and thus a reduction of the speed of sound in the downstream chamber as discussed in Fig. 13. However, cold unburnt gases sometimes reach the nozzle in the results by Urbano et al. [37], as reported, which gives a continuously increasing speed of sound in the whole chamber and thus a quick damping of pressure amplitude along the axial direction.

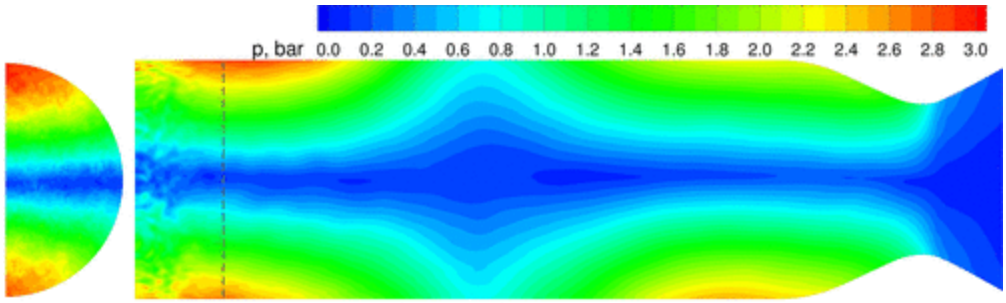

a) FFT

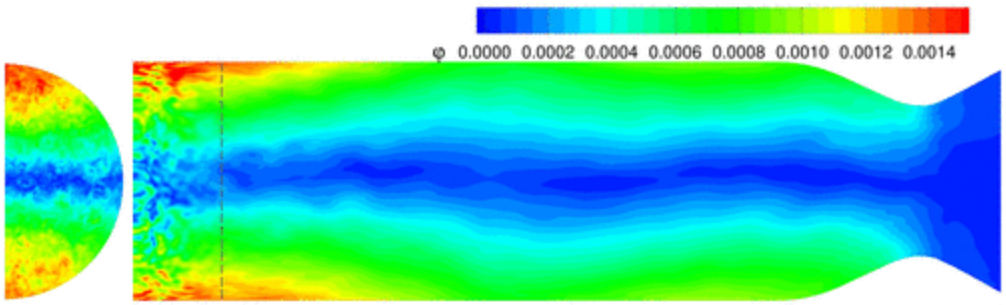

b) DMD

Fig. 14

Contours of 1T mode shape in chamber. Left: transverse slice at $x = 30$ mm; right: cylindrical wall surface.

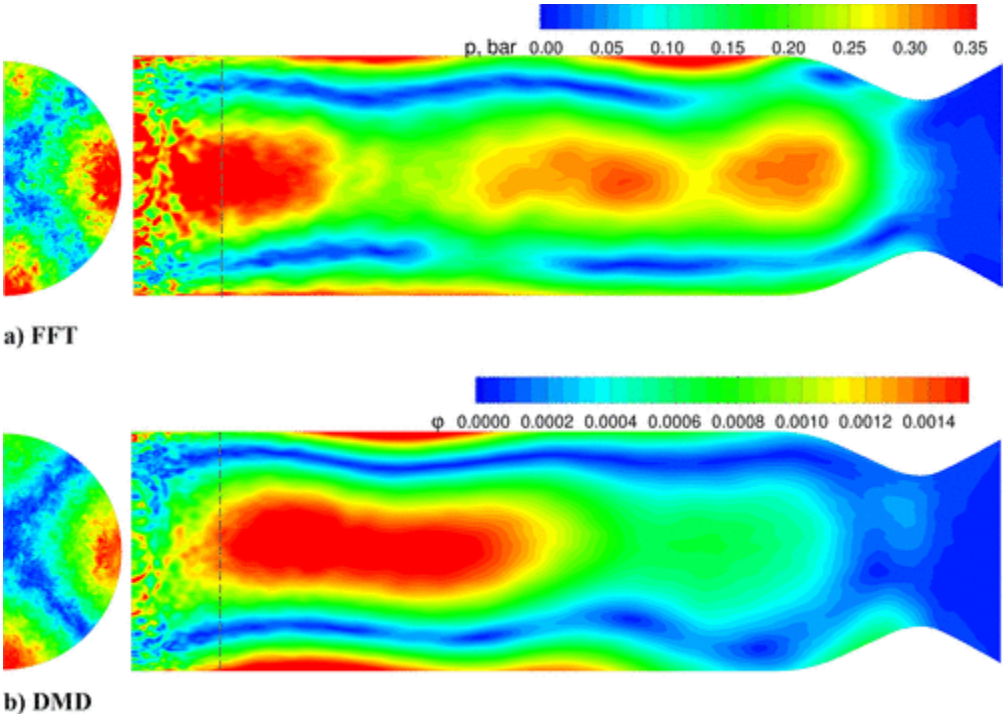

Fig. 15

Contours of 2T mode shape in chamber. Left: transverse slice at $x = 30$ mm; right: cylindrical wall surface.

One of the differences between FFT and DMD is that a zero point appears in the chamber middle for the 1T mode by FFT, as shown in Fig. 14a. This implies that the 1T mode by FFT is slightly modulated by the 1L mode. Although modulation is expected in both FFT and DMD due to their nature as linear approximations of a nonlinear acoustic system, their behaviors show slight differences. By assuming a constant speed of sound in the chamber, the theoretical solution to Eq. (18) estimates the frequency difference between the 1T and 1T1L modes to be approximately 430 Hz, which is smaller than the FFT frequency resolution of 500 Hz in the present case. Hence, the 1T mode is inevitably modulated by the 1L mode. In contrast, the frequency difference between the 2T and 2T1L modes is over 1000 Hz, higher than the FFT frequency resolution. The 2T mode by FFT is thus not modulated by the 1L mode, as shown in Fig. 15a. In DMD, however, each mode frequency is decided by the eigendecomposition process, rather than specified by the frequency resolution and its mode order. As a result, a DMD mode with an individual frequency can be identified, as indicated by the two tangential modes in Figs. 14b and 15b. The 1T mode shape by DMD is slightly different from the result by Hwang et al. [40]. Their DMD mode shape is most likely a 1T1L mode. Hwang et al. [40] did not provide the 2T mode shape in their analysis.

To quantitatively compare the tangential modes by FFT and DMD, Fig. 16 presents the variations of the modulus and real part of the 1T and 2T modes along the chamber wall at $x = 30$ mm. These tangential modes are standing waves along the azimuthal direction as indicated by the almost zero pressure amplitudes at nodal points. The high-order oscillations on the wave shapes are attributed to the effects of upstream injectors. Further downstream, the mode shapes become smooth, as shown in Figs. 14 and 15. The nonsymmetric behavior of a wave shape originates from the nonsymmetric

configuration of injectors on the half-chamber domain. It lasts until the chamber exit.

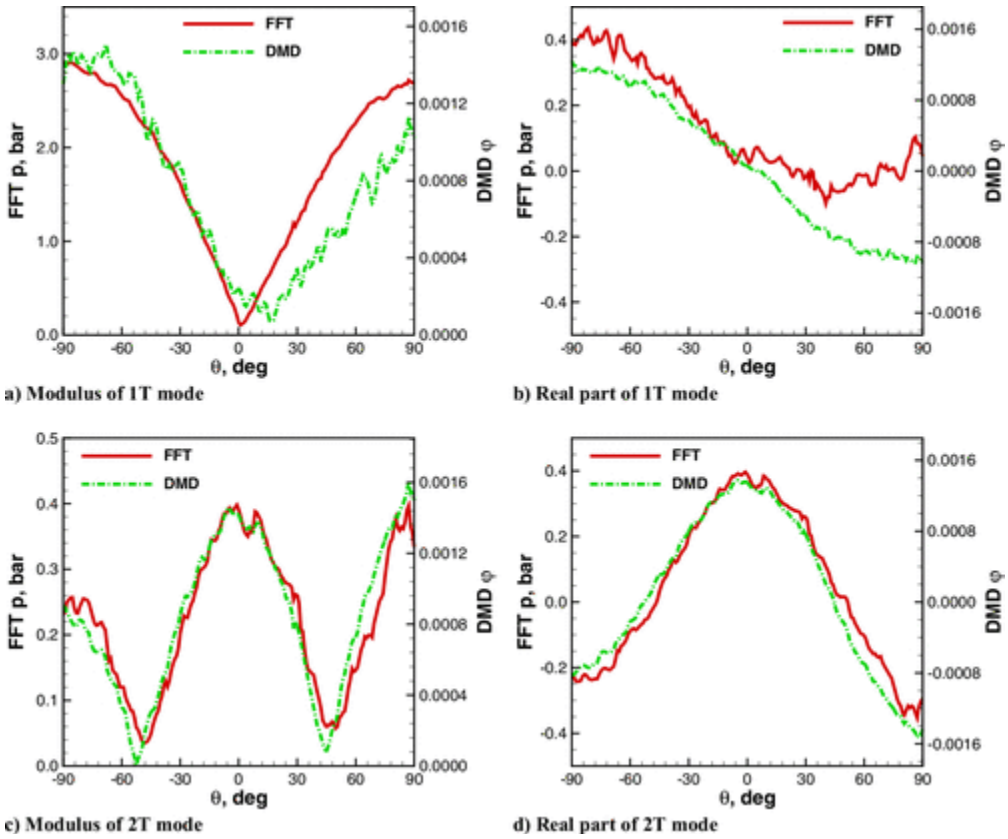

Fig. 16

Variation of tangential mode shape along chamber wall at $x = 30$ mm.

The first radial mode in the chamber is also presented. The contours of the 1R mode shape in the chamber is shown in Fig. 17, the right part of which is the symmetry plane of the chamber, while the left part is a transverse slice at $x = 30$ mm. Again, both FFT and DMD capture approximately the ideal mode shape of the Helmholtz equation, i.e., the zeroth-order Bessel function along the radial direction for the 1R mode. Along the axial direction, the pressure amplitude decays. Different from the longitudinal and tangential modes above, the 1R mode does not display an obvious rerise in the right half of the chamber. This may be attributed to the high frequency and low fluctuation amplitude of the 1R mode, which make it more susceptible to damping by turbulent fluctuations and viscous effects. The 1R mode shape closely aligns with the results by Urbano et al. [37] using FFT and solving the Helmholtz equation. However, their 1R mode decays more quickly along the axial direction for the same reason as the 1T mode. The DMD results by Hwang et al. [40] show a mixture of the 1R and 2R modes at the frequency of 21.5 kHz. The 2R mode is attached to the chamber entrance, while two 1R modes are located downstream of the chamber. We do not observe an evident 2R mode in the chamber.

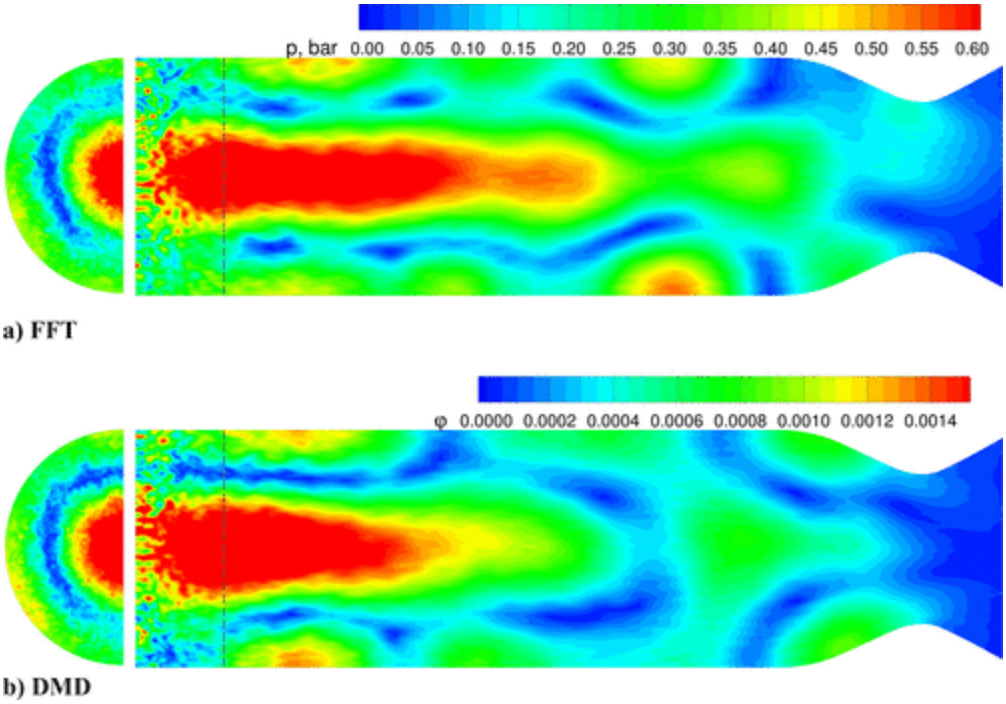

Fig. 17

Contours of 1R mode shape in chamber. Left: transverse slice at $x = 30$ mm; right: symmetry plane.

The variations of the modulus and real part of the 1R mode along the radial direction on the symmetry plane at $x = 30$ mm are shown in Fig. 18. Along the radial direction, the zeroth-order Bessel function decreases from a peak at the center, crosses the zero point, and reaches a 60% smaller negative peak at the end wall. Both FFT and DMD capture this variation along the radial direction. Compared to the tangential modes in Fig. 16, the 1R mode presents some degree of symmetry in the radial direction, which is kept until the chamber exit, as shown in Fig. 17.

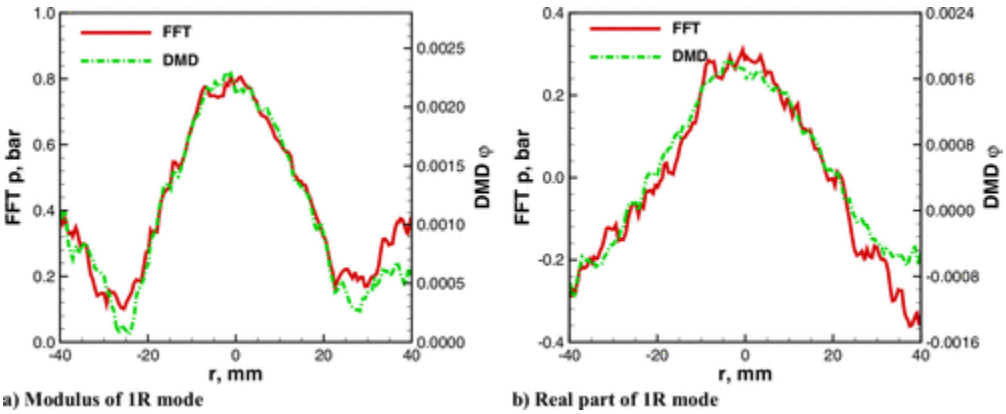

Fig. 18

Variation of 1R mode shape along chamber radius at $x = 30$ mm.

FFT can give the absolute value of pressure fluctuation for each mode besides its frequency and mode shape. Table 3 summarizes the mean-to-peak amplitude levels of pressure fluctuation obtained by FFT for acoustic modes examined in this section. For the three longitudinal modes, the pressure

amplitude level reduces as the mode order increases. A similar trend is observed for the two tangential modes. It is thus deduced that the amplitude of the 3T mode is much lower than that of the 2T mode, possibly at the level of acoustic noises. This is why a clear 3T mode shape is not captured by the present simulation. Among these primary acoustic modes, the 1L, 1T, and 1R modes have an amplitude over 1% mean chamber pressure. The 1T mode is in an absolutely leading position among these modes, followed by the 1L mode. This is consistent with the amplitude spectrum at specific grid points in Fig. 10. The 1T mode, with an amplitude of 3.75% mean chamber pressure, has the same pressure oscillation amplitude level as the experimental measurement by Gröning et al. [26]. It is lower compared to the oscillation amplitude of over 10 bar by Urbano et al. [37].

D. Instability Mechanism

Acoustic instabilities in a rocket engine chamber are closely coupled with the combustion in it, specifically the fluctuations of heat release rate. The combustion instability in a rocket engine is categorized into two types: intrinsic and injection-coupled processes [69], based on the underlying causes of volumetric heat release rate oscillations. Intrinsic instability arises when heat release rate fluctuations are caused by acoustic oscillations in the combustion chamber. In contrast, injection-coupled instability occurs when these fluctuations are induced by the propellant injection system. The BKD combustor experiment conducted by Gröning et al. [26] revealed that the heat release rate in the chamber oscillates exclusively at the resonant frequencies of the oxygen injector rather than those of the combustion chamber, indicating that the engine exhibits injection-coupled instability. They also demonstrated that a necessary condition for the onset of instability is that the 1T frequency of the chamber is close to the 2L frequency of the oxygen injector. This conclusion is supported by the LES study of the same engine conducted by Urbano et al. [37], which revealed that the longitudinal mode in the oxygen injector exhibits a $3/2$-wave (3L mode) structure at the frequency of the 1T chamber mode. Both experimental and numerical studies indicate that the tangential instability in the chamber is associated with a specific longitudinal mode in the oxygen injector.

The longitudinal modes in the oxygen injector are thus analyzed. In one-dimensional acoustics, pressure fluctuations are maximal and velocity fluctuations are zero at a closed end, whereas minimal pressure fluctuations and maximal velocity fluctuations occur at an open end. Perturbed by the strong pressure oscillations from the chamber volume, the downstream side of the oxygen injector can be reasonably viewed as a closed end, although we allow flow there. The upstream side is constrained by a fixed mass flow rate in the LES computation and therefore cannot be simply described by either an open or closed end. Instead, an appropriate impedance boundary condition must be applied at the upstream end, causing the injector to be between the limit cases of the open–closed and closed–closed tubes. The variations of the oscillation modulus, imaginary part, and phase angle of the 1L pressure mode along the oxygen injector centerline are obtained using FFT and shown in Fig. 19. The oxygen injector located near the amplitude peak of the 1T chamber mode, marked in red in the lower-right corner of Fig. 19, is selected for analysis. The FFT frequency of the 1L mode in the oxygen injector is $f_{\mathrm{ox,1L}} = 1.75\ \ \mathrm{kHz}$. The 1L mode exhibits a predominantly standing wave with a

weak traveling wave component, characterized by pressure amplitude peaks at both ends and a shallow minimum near the midpoint. The variation of phase angle further confirms the dominance of the standing wave. In theory, the phase angle of a standing wave remains constant along the centerline, with a possible abrupt jump of π at a node [8]. In the present case, it remains nearly constant at $3\pi/2$ on the right half of the port and shifts to $\pi/2$ on the left half. The slight nonlinear variation in the phase angle indicates the presence of a weak upstream-traveling wave. Since the phase angle in the injector is close to $\pi/2$ or $3\pi/2$, the imaginary part, obtained by multiplying the modulus by the sine of the phase angle, dominates over the real part and thus represents the signed waveform within the injector. It exhibits a cosine-like waveform within the injector tube. For the 1L mode, both ends of the injector tube appear to behave as closed ends, and the wave inside it is thus a half wave. The distance between the downstream pressure antinode and the phase-jump location, approximately 42 mm, corresponds to a quarter of the wavelength. Meanwhile, the gaseous oxygen of 230 K gives a theoretical sound speed of $290\ \mathrm{m/s}$. As a result, the 1L frequency in the oxygen injector is estimated as 1.73 kHz, consistent with the value by FFT.

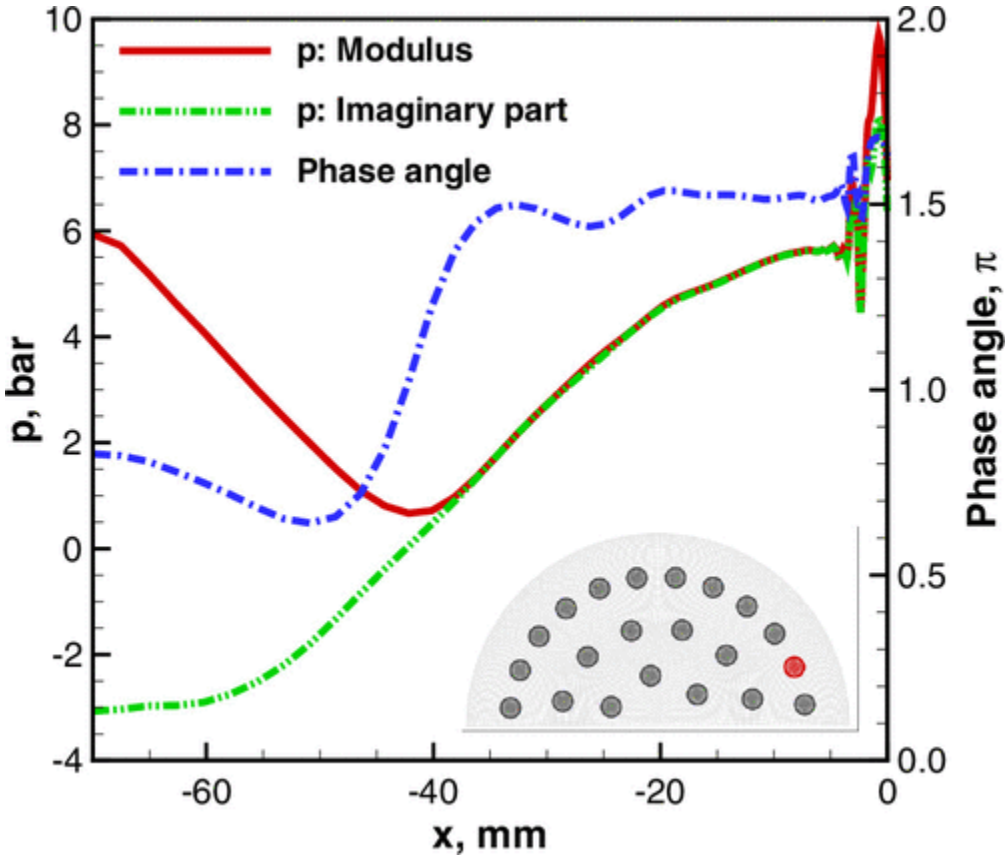

Fig. 19

Variation of 1L pressure mode along oxygen injector centerline.

Figure 20 shows the variation of the pressure oscillation along the oxygen injector centerline at the frequency of 11.75 kHz, corresponding to the 1T frequency in the chamber, $f_{cc,1T}$. The absence of pressure nodes suggests that this mode is most likely a traveling wave. This is confirmed by the

variations of the phase angle. In theory, the phase angle of a traveling wave varies linearly by 2π over one wavelength, and the wave propagates toward the direction of increasing phase angle [8]. The phase angle in Fig. 20 decreases linearly along the axial direction, indicating an upstream-traveling wave in the injector. The nonlinear variation of the phase angle near the injector inlet (between $x = -70$ mm and $x = -50$ mm) implies the presence of wave reflection at the upstream end. Moreover, the reflection appears to be weak, as its influence is confined to the vicinity of the inlet. The phase angle changes by $7/2 \cdot 2\pi$ over the entire length of the oxygen injector, indicating a $7/2$-wave mode. This is also evidenced by the presence of 3.5 wavelengths in the port, as indicated by the real or imaginary parts of the mode. The imaginary part leads the real part by a quarter of a wavelength. All suggest that this wave corresponds to the 7L injector mode. Recalling that its frequency is equal to the 1T chamber frequency, this indicates that the 1T frequency in the chamber matches the 7L frequency in the oxygen injector, i.e., $f_{\mathrm{cc,1T}} = 7f_{\mathrm{ox,1L}}$. This is similar to the experimental observation by Gröning et al. [26]. In their experiment, it is the 2L injector mode that matches the 1T chamber mode. This finding is also supported by the LES study conducted by Urbano et al. [37], where the 1T chamber mode matches the 3L mode in the oxygen injector. Hence, we can now deduce that the 1T frequency in the BKD chamber matches one of the harmonics of the longitudinal modes in the oxygen injector. Different longitudinal harmonics are observed across these three cases due to variations in the fundamental frequencies of the oxygen post, induced by the temperature of the fluid in it and, consequently, the speed of sound. The liquid oxygen used in the experiment [26] and the LES study by Urbano et al. [37] has a higher speed of sound compared to the perfect-gas oxygen modeled in the present simulation.

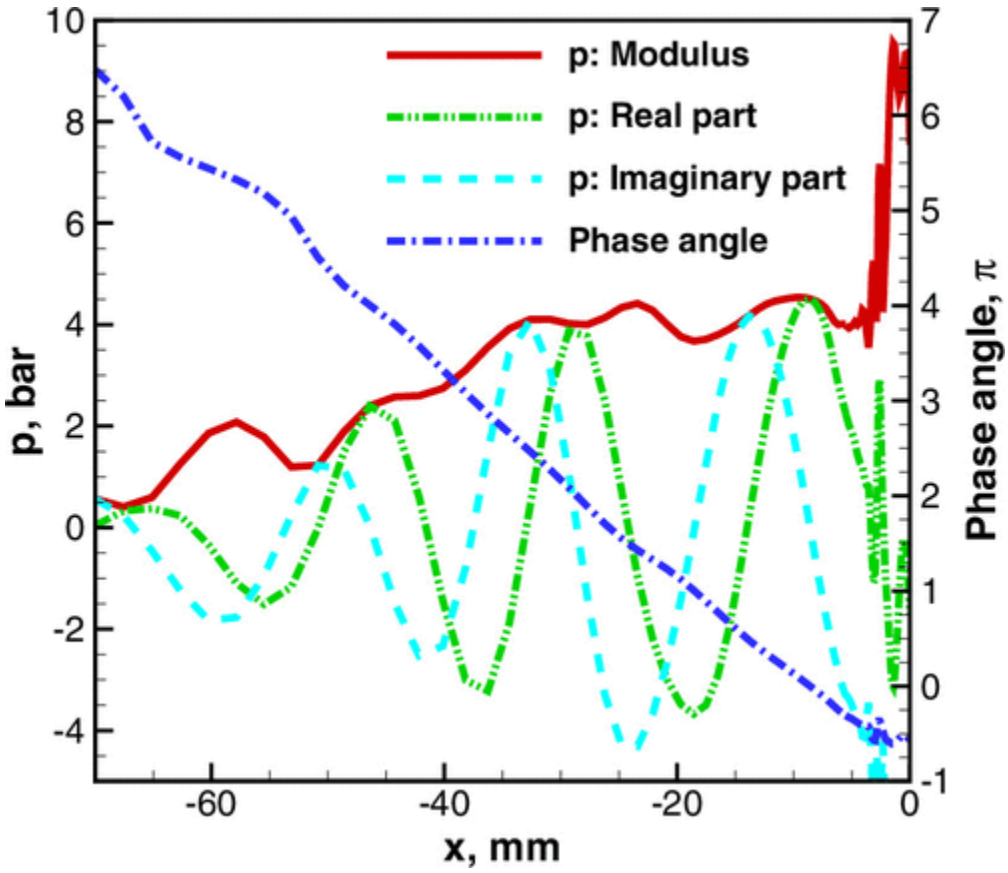

Fig. 20

Variation of pressure oscillation along oxygen injector centerline at the 1T chamber frequency.

In Fig. 20, the pressure oscillation amplitude exhibits an overall decreasing trend from the recess region to the injector inlet. Similar phenomena were also observed in the oxygen post of the CVRC configuration by LES [17,21,24]. This behavior is attributed to nonlinear waves propagating in the oxygen post [46]. It can be explained by the variations of pressure along the oxygen injector centerline at different time instants, as shown in Fig. 21. At $t = 3.42\ \ \mathrm{ms}$, a sharp and strong wave, nearly discontinuous, arises in the recess region. As time progresses, this wave propagates upstream toward the injector inlet. During this process, its strength gradually diminishes and its shape becomes smoother due to viscous dissipation within the oxygen shear layer. This explains the decay behavior in the pressure oscillation amplitude observed in Fig. 20. This also implies that the pressure oscillation near the injector inlet is too weak to generate a significant reflection at the inlet. At $t = 3.512\ \ \mathrm{ms}$, a new sharp and strong wave is generated in the recess region. The time interval between the two successive waves is 0.092 ms, corresponding to a frequency of 10.87 kHz, which closely matches the 7L injector frequency and thus the 1T chamber frequency. This suggests that the 7L pressure fluctuations in the oxygen injector are excited by the 1T acoustic mode in the chamber. However, no significant resonance occurs because of the weak reflection at the upstream end. It can be concluded that modification of the length of the injector post would change the frequency, but damping of the wave would still prevail. Consequently, the length of the post in the computation should not have a significant effect on the chamber acoustics. Wave reflection from the injector is not important at the injection temperature used here.

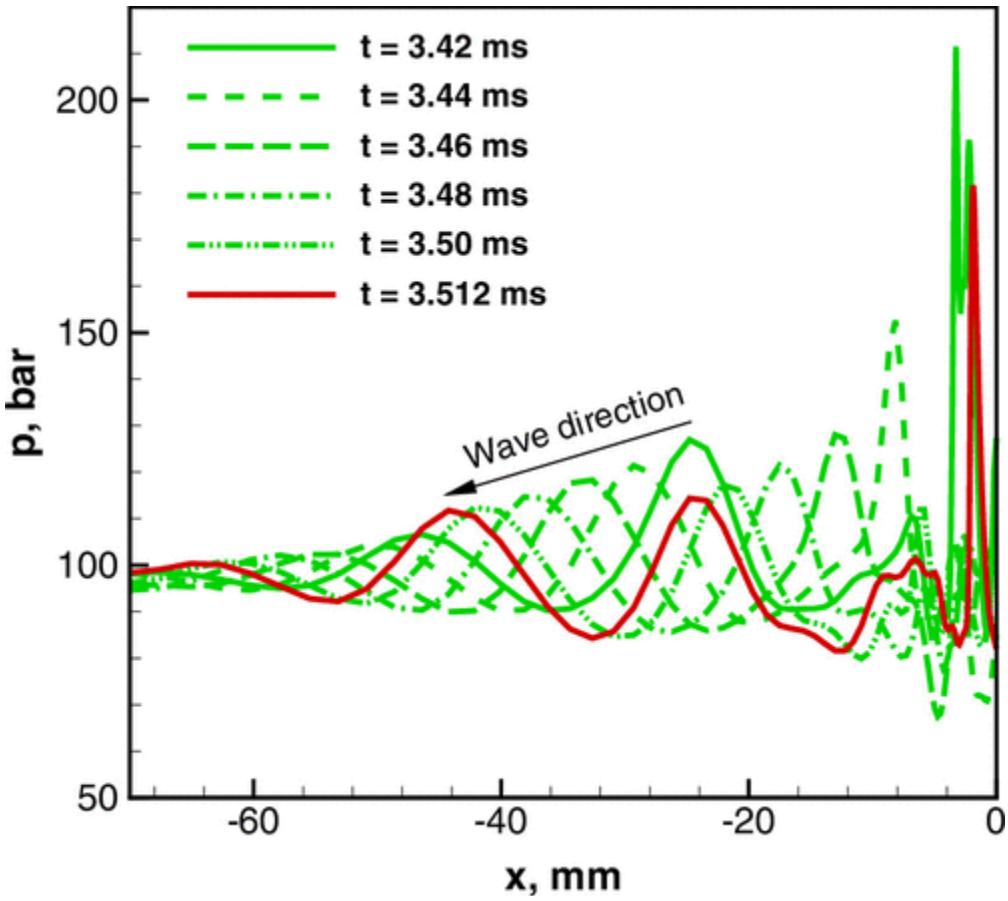

Fig. 21

Variations of pressure along oxygen injector centerline at different time instants.

The decaying and reflection behaviors of longitudinal acoustic waves in the oxygen injector are examined further. Figure 22 shows the variations of pressure oscillation modulus along the oxygen injector centerline at three injection-port resonant frequencies. The oscillation amplitude of the 7L injector mode strongly decays toward the upstream end with larger amplitude near the downstream end. In contrast, the comparable amplitudes observed at both ends for the 1L and 2L modes suggest that the two lower-order acoustic modes experience less attenuation within the oxygen injector. The presence of amplitude troughs in the 1L and 2L mode shapes indicates the existence of standing wave components, implying significant wave reflections at both ends of the injector. In contrast, the 7L mode, characterized as a traveling wave excited by the chamber, exhibits weak reflection at the upstream end, as discussed in Fig. 20. In summary, lower-order acoustic waves in the oxygen injector exhibit weaker decay and stronger reflection behaviors. This can be expected, since the higher modes have steeper gradients due to shorter wavelengths; therefore, the ratio of the viscous dissipation rate to the kinetic energy is higher for those shorter wavelength modes, regardless of the amplitude of each mode. If liquid propellants existed in the injectors, the sound speeds and wavelengths would be larger. Thereby, viscous dissipation would be decreased, making wave reflection at the upstream end of the injector more significant and increasing the importance of injector coupling.

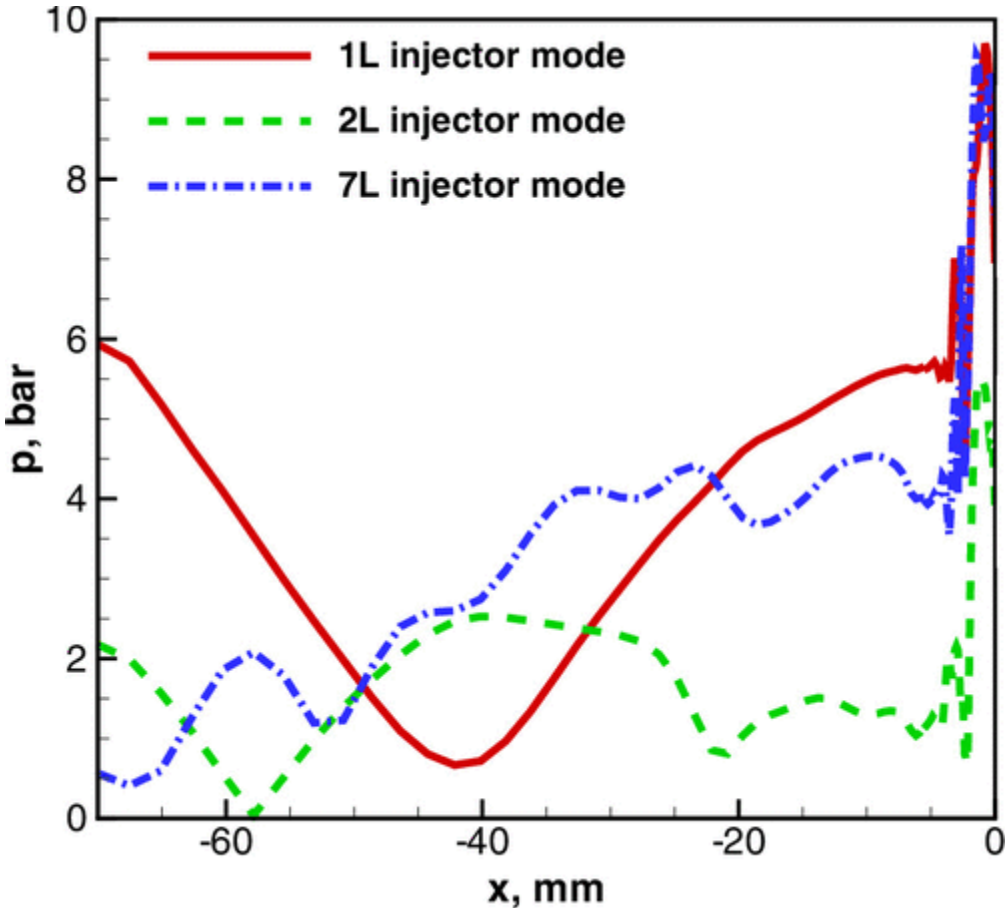

Fig. 22

Variations of pressure oscillation modulus along oxygen injector centerline at three injection-port resonant frequencies.

The amplitude spectra of the mean pressure and mean heat release rate in the chamber are shown in Fig. 23. The mean heat release rate oscillates by a fundamental frequency of 2 kHz. The first and second harmonics, at frequencies of 2 and 4 kHz, respectively, exhibit dominant amplitudes among all harmonic components. The fundamental frequency is close to the 1L injector frequency (1.75 kHz), i.e., $f_{\mathrm{cc},\dot{Q}} \approx f_{\mathrm{ox,1L}}$. None of the combustion chamber resonant frequencies (see Table 2) appear as dominant components in the heat release rate oscillations. This suggests that the oscillations of the heat release rate are created by the injectors rather than by the combustion chamber. The combustion instability in the BKD combustor is thus classified as injection coupled. This finding is consistent with the conclusion drawn from the experiment by Gröning et al. [26]. Although high-frequency acoustic modes, such as 1L, 1T, and 1R, are present in the chamber along with high amplitudes, the mean chamber pressure oscillations are dominated by low-frequency components. In addition, its dominant frequency closely matches that of the mean heat release rate, indicating that the global pressure fluctuation in the chamber is driven by the combustion process. This type of low-frequency instability originating from the coupling between the injector system and the unsteady heat release is referred to as chugging instability [7]. With chugging, the chamber pressure is nearly uniform across the combustor (due to a long wavelength) but oscillating in time. The mass flow exiting the nozzle and the thrust can be expected to oscillate at the chugging frequency.

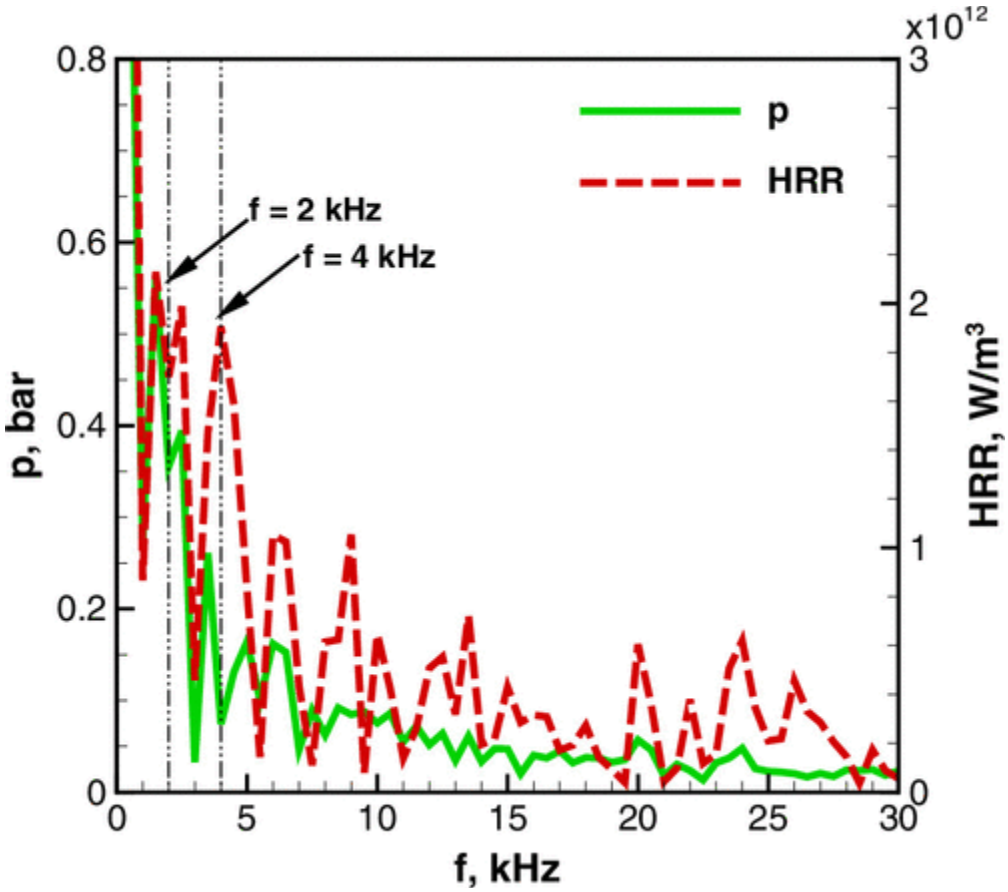

Fig. 23

Amplitude spectra of the mean pressure and mean heat release rate in chamber.

The above discussions examine the frequency relationship among the longitudinal acoustic modes in the oxygen injector, the mean heat release rate, and the 1T tangential mode in the chamber, i.e., $f_{\mathrm{cc},\dot{Q}} \approx f_{\mathrm{ox,1L}}$ and $f_{\mathrm{cc,1T}} = 7f_{\mathrm{ox,1L}}$. It can thus be deduced that $f_{\mathrm{cc,1T}} \approx 7f_{\mathrm{cc},\dot{Q}}$; the 1T chamber frequency approximately, but without consequence, corresponds to the seventh harmonic of the mean heat release rate oscillations. The alignment between the chamber pressure oscillation frequency and a harmonic of the heat release rate oscillations is a necessary condition for satisfying the Rayleigh criterion. The phase relationship between the acoustic waves in the chamber and the heat release rate can be quantified by the Rayleigh index, which further explains the dynamic mechanism of combustion instabilities in the rocket combustor. For linear acoustics at a low Mach number, the Rayleigh index in a specific volume Ω is defined as [8]

$$\mathrm{RI} = \frac{1}{\tau}\int_{\Omega}\frac{\gamma-1}{\gamma\bar{p}}\int_{\tau} p'(\boldsymbol{x},t)\dot{q}'(\boldsymbol{x},t)\,\mathrm{d}t\,\mathrm{d}\Omega \tag{21}$$

where τ is the period of the instability, $p'(\boldsymbol{x},t) = p(\boldsymbol{x},t) - \bar{p}(\boldsymbol{x})$, $\dot{q}'(\boldsymbol{x},t) = \dot{Q}(\boldsymbol{x},t) - \bar{\dot{Q}}(\boldsymbol{x})$, and γ is the specific heat ratio. The Rayleigh index provides a measure of the power fed by combustion to the acoustic field, with its sign indicating whether the combustion drives or dampens acoustic oscillations.

If the pressure oscillates in phase with the heat release rate, the resulting positive RI acts as a source term for the acoustic energy, and the flow is more likely unstable.

Figure 24 shows the history of the mean pressure and mean heat release rate in the chamber. The unsteady heat release rate is almost in phase with the pressure, with a slight phase lag. This implies a positive Rayleigh index in the chamber with a low frequency in the chugging range.

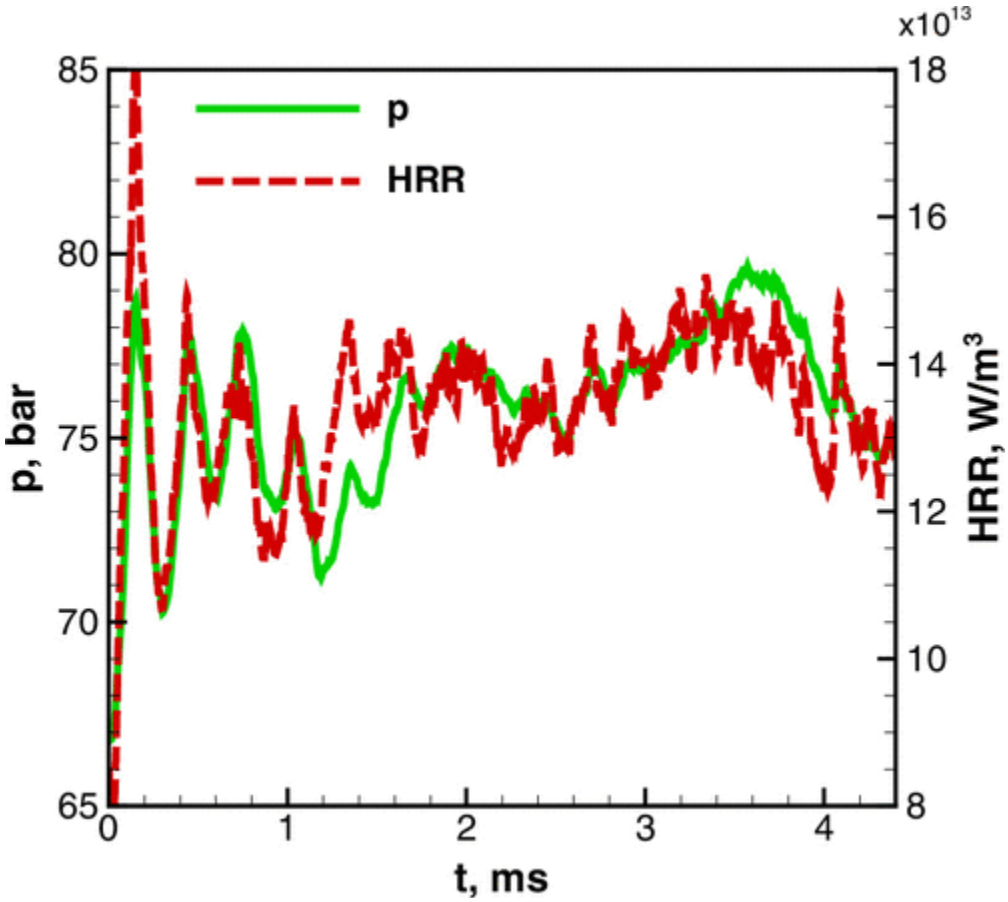

Fig. 24

History of the mean pressure and mean heat release rate in chamber.

The phase difference between mean pressure and heat release rate only provides a qualitative approach to predict global instabilities in the chamber, while the local Rayleigh index gives a quantitative criterion to identify the instability of an individual resonant mode. The contours of the local Rayleigh index in the chamber are shown in Fig. 25, the right part of which is the symmetry plane of the chamber, while the left part is a transverse slice at $x = 30$ mm. The local Rayleigh index is computed for every 64 computational cells over 2 ms by using Eq. (21). Gaps between adjacent blocks in Fig. 25 are because the Rayleigh index is defined on cell centers instead of on cell vertices. The large positive Rayleigh index regions appear in the first half of the chamber. This is consistent with the high-pressure oscillations in the first half for all primary resonant modes discussed in Sec. III.C. It is also consistent with the fact that strong chemical reactions happen near the chamber entrance. In the first half of the chamber, the large positive Rayleigh index is concentrated in the two corner regions between the chamber wall and the symmetry plane. The 1T mode has high-pressure oscillation

amplitudes in these regions, as shown in Fig. 14. This reveals that the standing 1T wave is triggered in the chamber and dominates the whole combustion instabilities because of the high enough Rayleigh index in the corner regions.

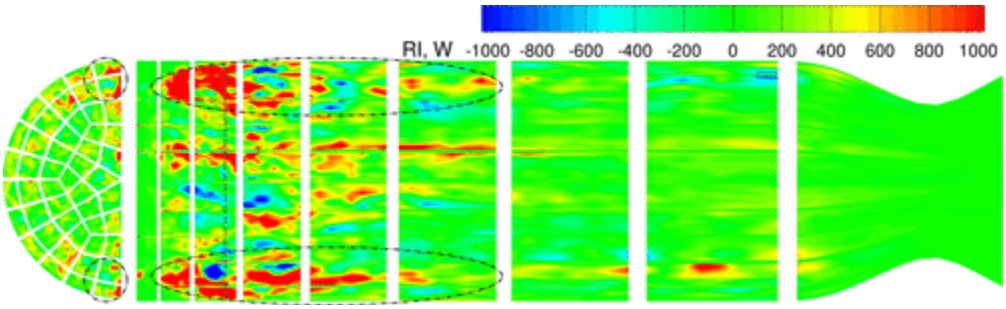

Fig. 25

Contours of Rayleigh index in chamber. Left: transverse slice at $x = 30$ mm; right: symmetry plane.

The sum of local Rayleigh indices within the chamber gives a global Rayleigh index of 36 MW. This positive value, consistent with the in-phase variations of pressure and heat release rate in Fig. 24, indicates that the combustion feeds energy into the acoustic fluctuations, resulting in unstable acoustic waves in the chamber. The global Rayleigh index is two orders of magnitude higher than 143 kW obtained by Urbano et al. [37] because the global reaction mechanism in this study is extremely strong and very sensitive to the temperature. This sensitivity can be seen from the stronger oscillation of heat release rate than that of pressure in Fig. 24. These results are consistent with the LES results of Xiong et al. [43] that one-step chemical kinetics overpredict the reaction rate and thus temperature compared to the experimental finding of Jensen et al. [45].

IV. Conclusions

The chemically reacting flow in the DLR BKD engine, an experimental hydrogen–oxygen rocket combustor, is simulated by using LES on multiblock structured hexahedral grids with a patched-grid interface between the chamber and injectors. A one-step finite-rate chemistry is applied to model the dynamic feedback process between combustion and acoustic oscillations. A half-cylinder of the rocket combustor is simulated along with a simplified propellant injection system by omitting the domes, throttles, and the upstream fuel injector section. To quickly establish the operation condition, a precursor solution is first obtained in a 60° sector domain and then transferred to the half-cylinder domain.

The primary acoustic waves in the chamber and exhaust nozzle, including 1L, 2L, 3L, 1T, 2T, and 1R modes, are identified by performing both FFT and DMD analyses on the unsteady pressure field. Both approaches obtain close results on the frequencies and corresponding mode shapes of these acoustic waves. It is identified that the combustion chamber exhibits a self-excited first tangential instability, which is consistent with the experimental measurement [27] and contrary to results of earlier computations by [37–40]. Attributed to the high temperature in the chamber, the computation obtains higher mode frequencies compared to the experiment [27]. The mode shapes, close to the

solutions to the homogeneous Helmholtz equation, quickly decay in the first axial half of the chamber and then gradually grow in the latter axial half. This is due to the speed of sound first increasing and then decreasing along the axial direction. Perturbed by the upstream injectors, mode shapes in the chamber exhibit intense oscillations up to 11 injector diameters downstream.

The mechanism of driving acoustic instabilities by combustion is explained by examining the longitudinal acoustic modes in the oxygen injector and the Rayleigh index in the chamber. The mean pressure and mean heat release rate in the chamber oscillate at approximately the frequency of the oxygen injector, unrelated to any resonant frequencies of the combustion chamber, indicating an injection-coupled chugging instability of the combustor. At lower resonant frequencies in the port, we do identify coupling of an acoustical oscillation in the port with a long-wavelength chugging frequency in the combustion chamber. This issue has not been addressed in prior literature. The 1T frequency in the chamber matches the 7L mode in the oxygen injector. This is similar to the experimental observation [26] and the previous numerical result [37], where the 2L and 3L injector modes were found to align with the 1T chamber mode, respectively. The heat release rate in the chamber varies almost in phase with the pressure, producing a positive global Rayleigh index and thus acoustic instabilities in it. The large positive Rayleigh index concentrates in the first axial half of the chamber, especially in the regions where the 1T mode oscillates with high amplitudes.

New insights are provided for the coupling with wave oscillations in the injector port. When a natural frequency (1T mode in the present study) of the combustion chamber occurs as a harmonic of that of the injection ports, waves from the chamber travel into the injection ports, inducing resonant oscillations within the ports, which in turn causes oscillations of the heat release rate in the reaction zone downstream of the injection plate. The frequency and phase synchronizations between the pressure and heat release oscillations heighten the Rayleigh index, strengthening the acoustic or chugging instabilities in the combustion chamber. This can be regarded as a significant contribution to the design engineer who wishes to avoid rocket engine combustion instability.

The influence of propellant temperature on the sound speed, wavelength, wave reflection at the upstream end of the port, and the viscous dissipation is better explained. The 7L pressure fluctuations in the oxygen injector are driven by the 1T acoustic mode in the chamber. However, major damping occurs in the injector port such that the reflection from the injector inlet is weak and the oxygen injector frequency has no consequence on the chamber acoustic oscillations at the temperature used here.

Acoustic oscillations are seen in the injector ports. However, the spontaneous first tangential mode is produced with comparable amplitude and frequency to the experiment [26] with highly dissipated injector-port oscillation at that frequency. The mass flux at the upstream end of the injector port is fixed and does not oscillate in our analysis. The collective injector-port space considered has about 40 times less volume and nearly an order of magnitude less mass than the combined combustion chamber and convergent nozzle space. Furthermore, for our analysis with warmer propellants and shorter wavelengths in the ports, the longitudinal port mode that matches frequency with the first-

tangential chamber mode is highly damped by viscosity due to its short wavelength. Consequently, there is no convincing evidence in our study that the coupling of the first tangential mode with the resonant oscillation has significance. The literature sometimes suggests the coupling is vital, but evidence has not been produced. Our findings suggest a different situation is possible; namely, the coupling can be one-way with the chamber oscillation driving the port oscillation. On the other hand, we do not claim that a stronger two-way coupling cannot exist at lower port-flow temperatures.

The overpredicted temperature, heat release rate, and thus Rayleigh index resulting from the one-step kinetics are expected to be improved by using more detailed chemical kinetics in future studies. Taking into account the propellant phase transition between liquid and gaseous states, along with reducing the injection temperature to realistic levels, can also help mitigate these overpredictions.

J. O'Connor, *Associate Editor*

Acknowledgments

This research was supported by the Air Force Office of Scientific Research through Grant FA9550-22-1-0191 with Dr. Justin Koo as program manager. This research was granted access to the high-performance computing resources of the U.S. Department of Defense and the San Diego Supercomputer Center. The authors are grateful to Dr. Justin Hardi in the Department of Rocket Propulsion Technology of the German Aerospace Center for providing the geometry and experimental data of the BKD rocket combustor.

Tables

Table 1 Mean stagnation pressure and temperature in combustion chamber

Parameter	Experiment	DLR	TUM	EM2C	ArianeGroup	IMFT	Present
P_0, bar	$81 \pm 1\%$	80	80	79.6	79	74.5	79.7
T_0, K	——	——	——	——	——	3180	3476

Table 2 Acoustic frequencies in combustion chamber (unit: kHz)

Parameter	1L	2L	3L	1T	2T	3T	1R
FFT	2.75	6.00	8.50	11.75	18.50	——	23.50

Parameter	1L	2L	3L	1T	2T	3T	1R
DMD	2.87	5.79	8.35	11.04	18.89	——	23.22
Urbano et al. [37]	——	——	——	10.70	——	——	21.40
Experiment	2.88	5.60	——	10.24	16.75	22.85	20.50

Table 3 Pressure fluctuation amplitudes of primary acoustic modes by FFT

Parameter	1L	2L	3L	1T	2T	1R
Pressure amplitude level, bar	1.0	0.4	0.2	3.0	0.4	0.8
Percent to mean chamber pressure, %	1.25	0.50	0.25	3.75	0.50	1.00

Previous Article Next Article